IPP-Report

Max-Planck-Institut
für Plasmaphysik

Sebastian Peterhansl

Stability of Tungsten Filaments in Hot Cathode Ionization Pressure Gauges

IPP 2020-15
November 2020


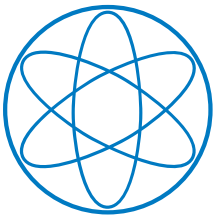


Bachelor's Thesis in Physics at
Technische Universität München

Stability of Tungsten Filaments in Hot Cathode Ionization Pressure Gauges

Sebastian Peterhansl

Garching, 02.11.2020

First Reviewer: Dr. Gregor Birkenmeier

Second Reviewer: Prof. Dr. Frank Pollmann

Supervisor: Dr. Michael Griener, Dr. Gregor Birkenmeier

Abstract

Nuclear fusion is a promising way to produce sustainable electric power. One possible way to achieve fusion in a power plant is the magnetic confinement of high temperature plasmas, which is applied in tokamaks and stellarators. For the operation of such fusion devices it is essential to know the parameters of the plasma-surrounding neutral gas for the protection of plasma facing components, as the neutral gas facilitates the reduction of heat loads due to line radiation and recombination processes. An important parameter of the neutral gas is the flux density as a measure for the pressure, which is measured by ASDEX pressure gauges at different locations inside the fusion device vessel. These pressure gauges are hot cathode ionization manometers with a linear cathode arrangement, optimized for the operation in the harsh environment of fusion devices with high magnetic fields. The electron emitting filament of the ASDEX pressure gauges is subject to a high mechanical load from the Lorentz force induced by the magnetic field of the fusion device and the heating current of the filament. This mechanical load, combined with the increased vulnerability of the filament material due to its high temperatures during operation, leads to plastic deformation of the filament due to creep processes and consequently causes a manometer failure.

To improve the lifetime of the filaments, a suitable combination of filament design and material has to be found, which, paired with the appropriate Lorentz force direction resulting from the heating current direction, should achieve a high resistance to creep processes. This Bachelor's thesis contributes to the search for a robust filament with an experimental examination of the stability of tungsten filaments of two different shapes, namely, the ear and meander design. For that, dedicated creep tests are performed, which simulate the mechanical stress acting on the filaments inside a tokamak by mimicking the Lorentz forces by means of a surrogate weight force in a dedicated laboratory experiment. The creep tests are performed with filaments formed from a 0.6 mm thick wire made of G18, which is tungsten doped with 1.8 % ThO_2, and ET4N, which is tungsten doped with 0.4 % ThO_2 and 70 ppm potassium. Both force directions are considered by operating the filament either at normal orientation or upside down.

The experiments showed that meander filaments perform better than ear filaments in terms of their stability. The comparison of the G18 filament creep tests with their ET4N counterparts showed a larger creep resistance of ET4N filaments compared to G18 filaments for small deformations. The ET4N meander filament with a downwards force direction was by far the most creep resistant filament of all tested configurations.

The consequence for ITER and other fusion experiments is that, if no superior filament design is found, the manometers should be equipped with ET4N meander filaments. These filaments have to be operated with a heating current direction leading to a downwards-facing Lorentz force on the filament.

Zusammenfassung

Kernfusion könnte in Zukunft einen großen Beitrag zu einer nachhaltigen Energieproduktion leisten. Tokamaks und Stelleratoren sind vielversprechende Konzepte für einen zukünftigen Kernfusionsreaktor. Sie basieren auf dem Prinzip des magnetischen Einschlusses, in dem das Plasma mithilfe magnetischer Felder eingeschlossen und gehalten wird. Das Plasma ist von neutralem Gas umgeben, welches eine große Relevanz für den Betrieb eines Fusionsexperiments hat, da es das heiße Plasma vor dem Kontakt mit der Wand durch Abstrahlung und Rekombinationsprozesse kühlt und damit die Wärmebelastung der Wandkomponenten reduziert. Um das Neutralgas steuern zu können ist eine Neutralgasdruckmessung erforderlich, welche von ASDEX Manometern an verschieden Positionen ausgeführt wird. Diese Druckmessgeräte sind Ionisationsmanometer mit einer linearen Elektrodenanordnung, optimiert für den Betrieb in einem Fusionsreaktor. Das Filament, welches für die Emission von Elektronen im Manometer verantwortlich ist, steht unter einer großen mechanischen Belastung durch Lorentzkräfte, die durch den Heizstrom im Filament und dem magnetischen Feld an der Manometerposition hervorgerufen wird. Diese Belastung kann zu einer Verformung des Filaments führen, welche durch die hohe Temperatur der Filamente begünstigt wird. Verformt sich das Filament über eine bestimmte Grenze hinaus, führt dies zum Versagen des Manometers.

Um die Lebensdauer der Manometer zu verbessern muss ein stabiles Filament gefunden werden, welches den Belastungen in einem Fusionsreaktor standhalten kann. Die Stabilität eines Filaments hängt überwiegend von drei Aspekten ab: Der Filamentform, dem Filamentmaterial und der Richtung der Lorentzkraft, welche durch die Heizstromrichtung beeinflusst werden kann. Diese Bachelorarbeit trägt mit einer experimentellen Untersuchung der Filamentstabilität zu der Optimierung des Filamentdesigns bei. Im Rahmen dieser Arbeit werden die Bedingungen in einem Fusionsreaktor durch Belastungstests nachgestellt. Dabei wird die Lorentzkraft mithilfe der Gravitationskraft durch ein entsprechendes Gewicht simuliert. Die Belastungstests werden für die zwei meistverwendeten Filamentformen, das sogenannte Ohrfilament und das Mäanderfilament, durchgeführt. Die Filamente werden aus G18- und ET4N-Woframdrähten mit 6 mm Durchmesser hergestellt. Der G18-Draht ist mit 1.8 % ThO_2 dotiert, während der ET4N-Draht neben einem 0.4 % ThO_2 Anteil 70 ppm Kalium beinhaltet. In den Belastungstests werden beide Kraftrichtungen getestet, wofür das Filament entweder bei normaler Ausrichtung oder kopfüber betrieben wird.

In den Experimenten haben die Mäanderfilamente eine bessere Stabilität gezeigt als die Ohr-Filamente. Für kleine Verformungsbereiche haben alle ET4N-Filamente besser abgeschnitten als die entsprechenden G18-Filamente. Das stabilste Filament ist das ET4N-Mäanderfilament bei einer nach unten gerichteten Kraft.

Für ITER und andere zukünftige Fusionsexperimente bedeuten diese Ergebnisse, dass die eingebauten Manometer mit ET4N-Mäanderfilamenten ausgestattet werden sollten, solange kein besseres Filamentdesign gefunden wird. Dabei sollte der Heizstrom zu einer nach unten zeigenden Kraftrichtung führen.

Contents

Chapter 1

Introduction

Thermonuclear fusion for energy production on earth can only be achieved in an environment of very high temperature and density, which has to be created and sustained in a plasma inside a fusion reactor [1]. One possible way to achieve such conditions is the magnetic confinement of the plasma, as used in tokamak and stellarator fusion experiments [2].

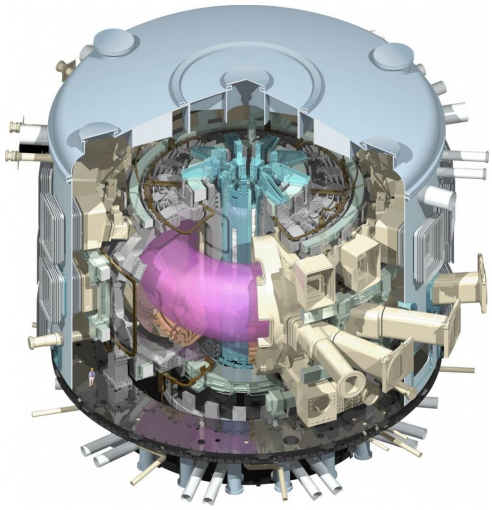

Figure 1.1: Model of the tokamak fusion experiment ITER [3].

The most important representative of a tokamak fusion experiment is the international project "ITER", under construction in the south of France, which is expected to be the first fusion device that will be able to generate a self heating plasma [4]. A schematic of ITER is shown in fig. (1.1). The tokamak experiment "ASDEX Upgrade", operated by the Max Planck Institute for Plasma Physics in Garching, is a fusion device smaller than ITER, but with similar configuration so that ITER relevant physics can be studied in great detail. This way, it significantly contributes to the development of a fusion reactor concept [2, 5].

For the operation of such fusion devices it is essential to know the parameters of the plasma and its surrounding neutral gas. The neutral gas inventory is important to know and control in a fusion device, since plasma facing components must not be overloaded by heat and particle fluxes from the plasma. This is in particular important for the divertor,

a region below the plasma where the hot plasma is in direct contact to wall components via magnetic field lines [6]. Only if a sufficient neutral gas inventory consisting of hydrogenic neutrals or seeded impurities is present, the divertor can be protected from harmful heat and particle fluxes [6]. In order to control these essential plasma regimes with high line radiation fraction and a detached divertor, a fast, local and reliable measurement of neutral gas properties is needed [7].

One important property of the neutral gas is the neutral flux density as a measure for the gas pressure, which is monitored by several manometers distributed in the plasma vessel, as shown in the poloidal cross-section of the ASDEX Upgrade tokamak (see fig. (1.2)). These pressure gauges have to endure exposure to high plasma confining magnetic fields with a strength up to 8 T, as it is the case in ITER [7]. Also, they need to be able to operate in an environment with a strong neutron flux and radiation, while providing a relative accuracy of at least 20 % [7]. The installation and operation of manometers outside the vessel to avoid magnetic fields and strong background noises is not an option due to the additional requirement of a sufficient time resolution, which cannot be met when using ducts to connect the gauges to the vessel [7].

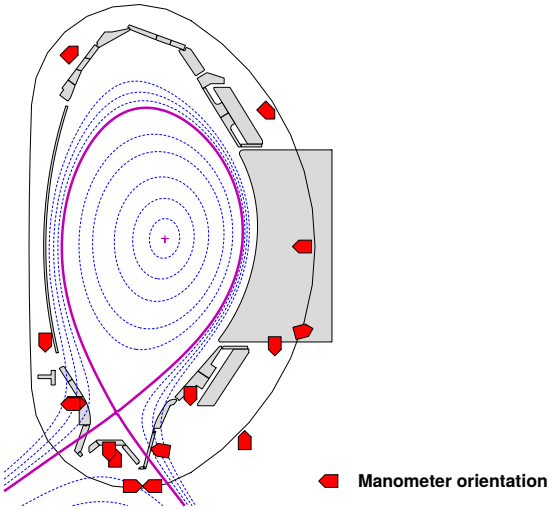

Figure 1.2: Poloidal cross-section of the ASDEX Upgrade tokamak. The blue dashed lines indicate flux surfaces and the magenta line represents the last closed flux surface, which is the outer boundary of the confined plasma [8]. Vessel components are shown in grey and the ASDEX manometer location and orientation in red.

Ionization pressure gauges are already in use for fusion applications [7]. These manometers measure the pressure by ionizing atoms with accelerated electrons, collecting the ions at an electrode held at a low potential and derive the pressure from the electron and ion currents. However, using conventional ionization pressure gauges, such as a Bayard-Alpert gauge, is not an option for the measurement of the neutral flux density in the fusion device vessel, as their cathode arrangement would lead to $\vec{j} \times \vec{B}$-Lorentz forces diverting the charged particles from their paths. A schematic of the electrode setup in a Bayard-Alpert gauge is shown in fig. (1.3).

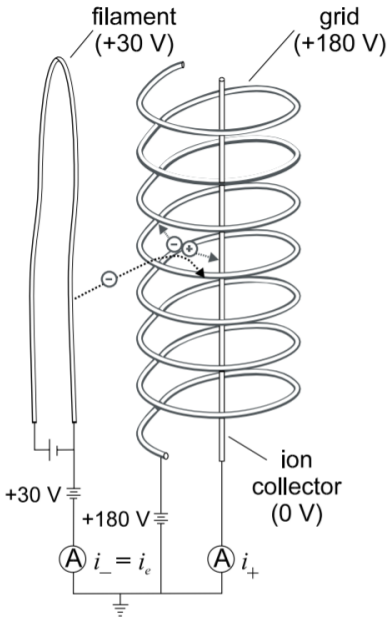

Figure 1.3: Schematic of the cathode arrangement in a Bayard-Alpert pressure gauge [9]. The filament (left) is heated and emits electrons which are accelerated by the grid (spiral). They ionize the volume inside the spiral and the resulting ions are collected by the ion collector rod in the center of the spiral.

This led to the development of the ASDEX pressure gauge starting in 1976, a hot cathode ionization manometer with a linear arrangement of its components, which is shown in chapter 2. This design can be aligned with the local magnetic field to prevent Lorentz forces diverting charged particles from their straight path inside the gauge. As this pressure gauge design is better suited for conditions inside fusion devices when compared to other types of manometers, the ASDEX pressure gauges are also used in other fusion experiments, such as the stellarator Wendelstein 7-X [7, 10].

However, one disadvantage of this design is a high mechanical strain on one of the components, the hot cathode, also referred to as filament. Due to the linear arrangement of the manometer components, the filament has to be oriented perpendicularly to the local magnetic field, leading to strong Lorentz forces acting on the filament. In combination with the high cathode temperatures required for electron emission, this leads to a plastic deformation of the filament due to fatigue and creep processes, causing manometer failure. This has to be avoided or at least minimized in ITER and future fusion experiments, since the pressure measurement from manometers is essential for the control of the plasma, and the replacement of in-vessel components like this manometers are cumbersome due to the mandatory use of remote handling [11].

After the discovery of this issue, the filament deformation was examined more closely and different approaches were tested to improve its stability. One important aspect is the filament design and its dimensions. This was addressed in ref. [12], where finite element analysis was carried out to simulate temperature distributions in the filament and to compare different filament shapes in terms of their stability for different wire diameters. The simulations in ref. [12] predicted the “ear” shape, which is shown and discussed in section 2.4, with a wire diameter of 0.8 mm to be the optimal filament design.

The cathode material is also a very important factor for the stability. The most common choice is tungsten, as this is the metal with the highest melting point of 3422 °C [13] and is thus expected to endure stresses even at high temperatures. Additionally, the work function of the filament is reduced by doping the tungsten with a second material such as ThO_2 or Re, which lowers the required cathode temperature for electron emission [12]. This consequently reduces the required heating current and thus, the Lorentz force acting on the filament. Filament coating can also be an option to adjust the work function, however it may dissolve after some operation time.

Some of the material comparisons are a part of ref. [14]. First, ref. [14] showed that creep is the main cause for cathode deformation, while failure due to material fatigue from repeated heating and cooling could not be observed. Additionally, ref. [14] included some stress tests for material comparison.

Other approaches such as heating the filament with an alternating current or changing the tungsten wire to a LaB_6 crystal, which has a low work function, have been tested as well [10, 15].

In this Bachelor's thesis, three open questions regarding the filament stability are addressed. First, the stability of the most common filament designs, the "ear" and the "meander" design, is examined. This is achieved with creep tests simulating the mechanical stress on filaments inside a fusion device. Second, the impact of the Lorentz force direction on the filament stability is tested. The Lorentz force acting on the filament can either face downwards or upwards, depending on the heating current direction in the filament. Third, the creep tests are performed for filaments made of two different materials. One material is G18, which tungsten doped with 1.8 % ThO_2 and the other material is ET4N, which is tungsten doped with 0.4 % ThO_2 and 70 ppm potassium. The potassium is supposed to improve its resistance to creep processes [16].

The manometer and filament design is explained in chapter 2, next to the causes of filament deformation and consequently, the manometer failure. In chapter 3, the creep test and the experimental procedure are described, followed by the evaluation of the experimental data and comparison of the filaments in chapter 4. Finally, chapter 5 concludes the project with a summary of the results and an outlook.

Chapter 2

Manometer design and working principle

2.1 Manometer electrodes

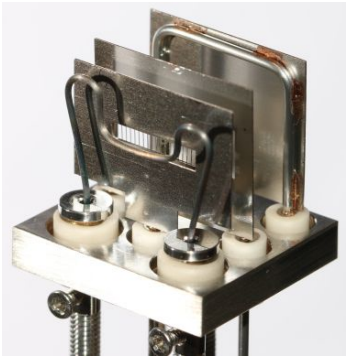

(a) Photograph of a pressure gauge [17].

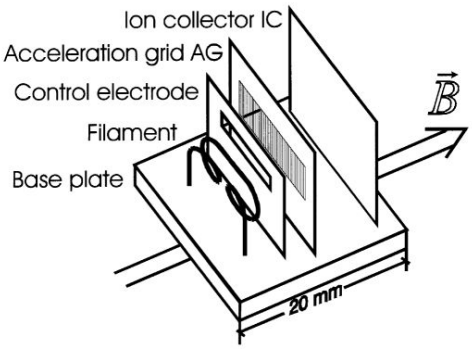

(b) Schematic of the manometer setup, adapted from [18].

Figure 2.1: Photograph of a manometer measuring head (a) and a schematic representation of the single components (b).

In this chapter the structure and working principle of an ASDEX pressure gauge is explained. First, the design and purpose of its components is discussed, followed by an explanation of the manometer measurement principle. After that, the manometer failure due to filament deformation is described and finally, the last section of the chapter concludes with a detailed description of the filament properties.

Fig. (2.1a) shows an open manometer head and fig. (2.1b) a schematic of the major manometer components. The manometer electrodes are mounted on the base plate with ceramic isolations. The general working principle of the manometer is the following: The filament emits electrons which are accelerated by the acceleration grid. A portion of about 20 % to 25 % are collected by the acceleration grid, leading to an electron current at the electrode. Collisions of neutral atoms with the electrons can create ions, which are collected by the ion collector if the ionization occurs between the ion collector and the acceleration grid. Using the electron current at the acceleration grid and the ion

current at the electrode, a neutral flux density can be derived, which is a measure for the pressure. To measure offsets in the ion signal, the control electrode is switched between two potentials, which in one case aligns with the potential across the manometer and in the other case is set very low to repel emitted electrons away from the manometer.

The filament is a tungsten wire formed in such a way that it has an approximately 1 cm long straight wire section at its center, as can be seen in fig. (2.2). The straight section is parallel to the base plate and the other electrodes and is located at a height of about 7 mm above its fixations. There are different filament shapes that can satisfy these conditions, the two most used designs, the "ear" and the "meander" filaments, are presented in the following section. Fig. 2.2 shows, as an example, a meander filament.

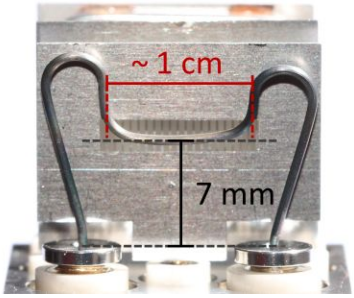

Figure 2.2: Dimension and position of the filament straight section, window of the control electrode behind the filament at approximately the same height with slightly larger dimensions, adapted from [17].

During manometer operation, the filament has to emit electrons, requiring high wire temperatures for thermal electron emission, as the electrons will overcome the work function of the material and exit the filament. Such temperatures can be reached by leading high currents through the cathode, as this produces ohmic heat due to the wire resistance.

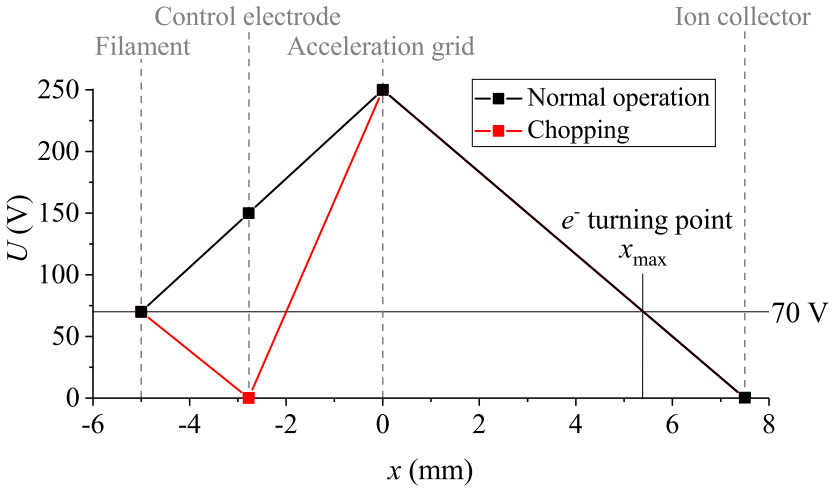

Figure 2.3: Potential curve across the manometer axis for two different states of the control electrode. Control electrode at 150 V during normal manometer operation (black) and at 0 V to chop the electron current for background measurements (red) [18].

The emitted electrons are accelerated towards the center of the manometer by the acceleration grid, which is at a potential of +250 V, while the filament is operated at +70 V. The acceleration grid is an electrode with thin, vertically arranged bars in a large window. This construction allows for about 75 % to 80 % of the emitted electrons to pass through, while the other $20 - 25$ % are collected by the grid, leading to an electron current at the electrode [18]. Since the operation of the manometer requires a stable, preset electron flux, the heating current is feedback-controlled by the electron current [18]. The emitted electrons then start oscillating between the filament and the ion collector, as the ion collector is set at a potential of 0 V and therefore repels the electrons back towards the acceleration grid. Since the filament is at a potential of +70 V, the electrons cannot reach the ion collector. The maximum distance $x_{\max} \approx 5.4$ mm the electrons can move away from the grid towards the ion collector is given by the position at which the potential reaches +70 V, as shown in fig. (2.3). When the electrodes are surrounded by neutral gas, the electrons can collide with the atoms and ionize them. The portion of ionization processes which occurs between the acceleration grid and the ion collector, which is called ionization volume, can be detected, as the created ions are repelled from the acceleration grid and collected by the ion collector, resulting in an ion current at the electrode [18]. Since the ionization rate is a function of the neutral gas and the electron density, the neutral gas flux density can be determined by means of the ion current for a given electron current. The measurement of the ion signal and the electron current therefore constitutes the raw data output of the manometer, which can be processed further to derive the pressure, as is shown in the following section.

The control electrode is an electrode with a small window at the height of the filament straight section with a width slightly higher than 1 cm, as can be seen in fig (2.2). The electrode can be set to +150 V or 0 V, which in the first case aligns with the linear potential increase between the filament and the acceleration grid, as can be seen in the black plot of fig. (2.3). In this configuration, the electrons can pass the control electrode through the window without being influenced. If the control electrode is set to 0 V, as shown in the red plot of fig. (2.3), the emitted electrons are repelled by the control electrode, leading to a collapse of the electron flux at the other electrodes. This process is called "chopping" and it is used to measure offsets of the ion collector signal due to background noise and leakage currents. The background measurements cannot be carried out by turning the filament off and on, as it can take a few seconds for the filament to cool down and stop emitting electrons and likewise, a few seconds to heat up again and provide the required electron emission current. The background measurements, however, typically have to be performed at a rate of 2 kHz, which leads to the necessity of the control electrode.

Figure 2.4: Photograph of a manometer head, covered by the protection cap with a hole which has a diameter of approximately 10 mm [17].

To protect the manometer components from fast charged particles during tokamak operation, the electrodes are covered by a metal box with a small hole on the top, as can be seen in fig. (2.4). This also makes the particle velocity distribution inside the pressure gauge independent from the conditions outside the gauge, since entering particles have to undergo many wall collisions leading to their thermalization, which is important for the derivation of the pressure from the raw data output of the manometer [18].

2.2 Measurement principle

In this section it is explained how the raw data output of the manometer, which is given by the electron current at the acceleration grid I_e and the ion current at the ion collector I_+, is processed to derive the pressure. By means of the ion current and the electron current, a neutral flux density F can be derived as

$$F = \frac{I_+}{(I_\mathrm{e} - I_+) \cdot d}\,, \tag{2.1}$$

where d is the manometer sensitivity [18]. The sensitivity is determined by a calibration measurement compared with an absolute pressure measurement, for example from a baratron [18]. The unit of the flux density is $1/\mathrm{m}^2\mathrm{s}$, which can be understood by looking at the general formula for the flux density

$$F = \frac{n}{A} \int_A \int_{-\infty, v_\mathrm{n}>0}^{\infty} f\left(\vec{v}\right) \cdot \vec{v} \cdot \mathrm{d}\vec{A} \cdot \mathrm{d}^3 v\,, \tag{2.2}$$

where A is the test surface, $\vec{v}$ the velocity of the neutral atoms, $f\left(\vec{v}\right)$ their velocity distribution and n the neutral particle density [19]. The condition $v_\mathrm{n} > 0$ means that only $\vec{v}$ with a positive velocity component parallel to the surface normal vector are considered to exclude particles which are moving away from the test surface [19]. Assuming a thermal velocity distribution $f\left(\vec{v}\right)$ of neutral particles in the manometer, the flux density becomes

$$F = n \cdot \sqrt{\frac{k_\mathrm{B} \cdot T}{2\pi \cdot m}}\,, \tag{2.3}$$

where k_B is the Boltzmann constant, T the temperature and m the mass of neutral particles [19].

Assuming that the neutral gas can be described by the equation of state for an ideal gas, the flux density can be used to calculate the pressure when the temperature is known. The connection is made by the particle density, as both the flux density and the pressure are proportional to n. The proportionality $p \propto n$ can be shown by the rearrangement of the equation of state for an ideal gas

$$p \cdot V = N \cdot k_\mathrm{B} \cdot T \tag{2.4}$$

$$p = n \cdot k_\mathrm{B} \cdot T \tag{2.5}$$

where V is the volume and N the number of particles, whereby the particle density is given by $n = N/V$. Replacing the particle density in eq. (2.5) with the rearranged eq. (2.3) results in

$$p = F \cdot \sqrt{2\pi \cdot m \cdot k_\mathrm{B} \cdot T} \overset{2.1}{=} \frac{I_+}{(I_\mathrm{e} - I_+) \cdot d} \cdot \sqrt{2\pi \cdot m \cdot k_\mathrm{B} \cdot T}\,. \tag{2.6}$$

The main fuel for the present-day fusion experiments are deuterium nuclei, therefore, many deuterium molecules D_2 are present in the neutral gas [2]. For the deuterium molecules, where the mass of a single deuteron D^+ is $m_\mathrm{D} = 2.0136\,\mathrm{u}$ [20], eq. (2.6) can be written as

$$p = 1.32 \cdot 10^{-23}\,\mathrm{kg}\frac{\mathrm{m}}{\mathrm{s}} \cdot \frac{I_+}{(I_\mathrm{e} - I_+) \cdot d} \tag{2.7}$$

when assuming room temperature of $T = 25\,^\circ\mathrm{C}$.

2.3 Filament deformation

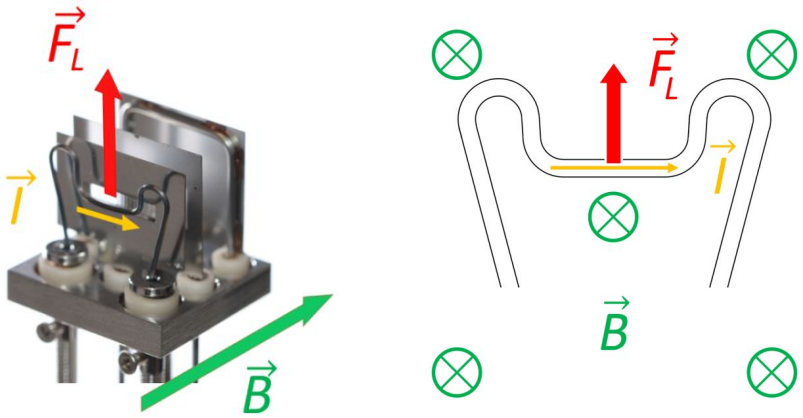

(a) View of the open manometer head, adapted from [17].

(b) Schematic view of the filament.

Figure 2.5: Orientation of the filament relative to the magnetic field and the resulting Lorentz force direction acting on the central part of the cathode for an example heat current direction.

As mentioned in the introduction, a serious issue with the ASDEX pressure gauges is failure due to deformation of the filament under fusion experiment conditions. The breakdowns are caused by the Lorentz force acting on the cathode, since the heating current is perpendicular to the local magnetic field, as shown in fig. (2.5). The central part of the filament usually suffers the most from the stress, as it is the hottest and therefore weakest part of the filament. However, errors such as bad contacts at the filament fixations or deviations from the ideal shape can shift the heat distribution, making it asymmetrical and thus changing the most vulnerable areas. Internal damages or inhomogeneities in the wire can also have a similar consequence or constitute an additional weak point regardless of the heat distribution.

The failure of the manometer due to filament deformation can either occur at the point at which the majority of emitted electrons can no longer pass the control electrode as shown in fig. (2.6), or when a contact of the filament with the control electrode occurs, forming a short circuit visible in fig. (2.7). In rare cases, the filament can also break, as can be seen in fig. (2.8).

This issue is further amplified by the feedback loop, as the deformation of the filament leads to an increasing amount of electrons hitting the control electrode instead of passing through its window. Since the amount of emitted electrons inside the manometer has to remain constant, the filament heating has to increase to compensate for the losses due to the deformation. This, however, also amplifies the load on the filament, as the Lorentz force rises with the heating current, which then results in an even faster creep process.

(a) Broken manometer head with an ear filament [17].

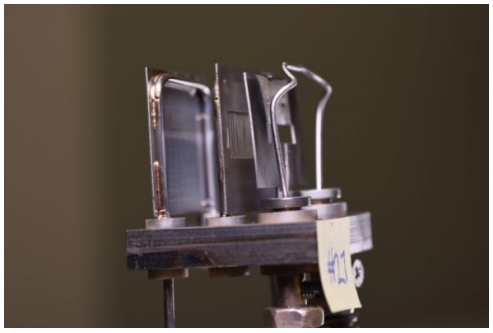

(b) Broken manometer head with a meander filament [17].

Figure 2.6: Examples of broken manometers from ASDEX Upgrade at the summer opening 2019, failure due to misaligned filament straight sections.

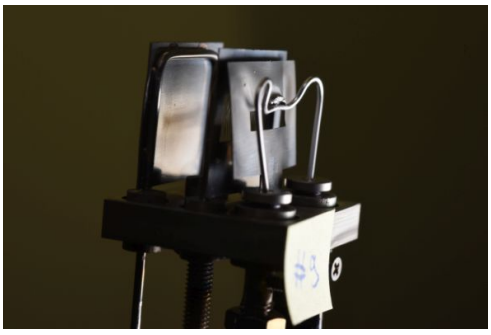

Figure 2.7: Example of a broken manometer from ASDEX Upgrade at the summer opening 2019, failure due to short circuit between the filament and the control electrode [17].

Figure 2.8: Example of a broken manometer from ASDEX Upgrade at the summer opening 2019, failure due to a partly disjointed filament [17].

2.4 Filament design

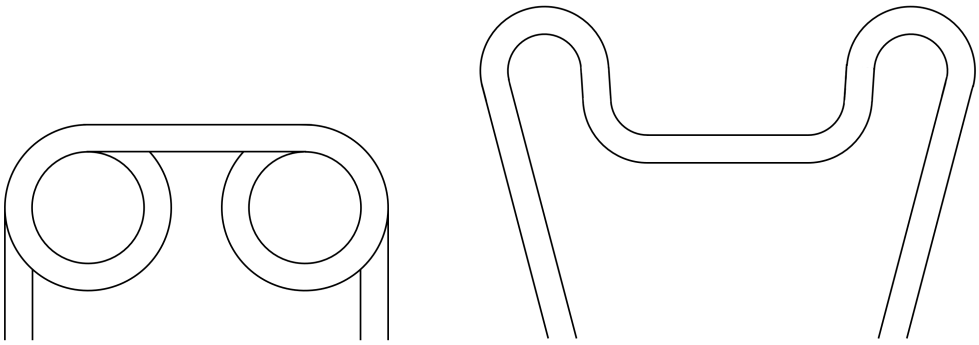

(a) Ear design (b) Meander design

Figure 2.9: Schemes of the filament designs used in ASDEX gauges.

In the previous section, it was explained how the filament deformation can shorten the pressure gauge lifespan. The solution to this problem requires finding a stable, creep-resistant material with a preferably low work function for the filament and a suitable filament design. There are currently two promising types of filament designs used for ASDEX pressure gauges, the ear- and the meander filament, which are displayed in fig. (2.9). The ear shape can be recognized by a single spiral on each side transitioning into the straight section, which makes the ear filament a 3D-structure. The meander filament on the other hand has a planar shape, with an arc on each side leading into the straight section at the center. The need for such complicated designs results from the issue that a portion of the heat is conducted to the sides of the wire, leading to a temperature gradient in the filament. An example simulation of such a temperature distribution can be seen in fig. (2.10) for a tungsten ear filament doped with 2 % ThO_2 and a wire diameter of 0.8 mm at a heating current of 20 A.

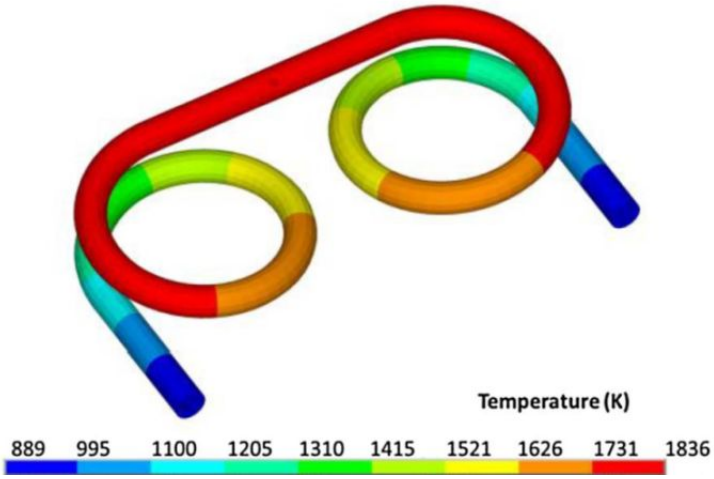

Figure 2.10: Simulated heat distribution of a tungsten ear filament doped with 2 % ThO_2 and a wire diameter of 0.8 mm at a heating current of 20 A [12].

To counteract the filament cooling, the wire length has to be high, as more wire leads to more heat created in the filament. This encourages using filaments with complicated shapes over simple shapes requiring less wire, like a rectangular filament for example.

The length of the filament wire, measured from one end of the fixation tube to the other, is approximately 49 mm for the ear shape and 40 mm for the meander shape. It therefore requires less heating current for the ear filament to reach a certain electron emission compared to the meander filament. It has to be noted that the full wire forming the filaments is actually longer than the mentioned values, since a part of the wire is inside the fixation tube, clamped by a screw perpendicular to the tunnel to hold the filament in place, as can be seen in fig. (2.1a). However, this is equal for both filament types, so the difference in wire length remains at approximately 9 mm.

Chapter 3

Filament creep test setup and procedure

For a detailed experimental comparison of the filament shapes dedicated creep tests were performed. The objective was to simulate the mechanical stress which the filament would experience during operation inside a tokamak and observe its deformation. However, it is difficult and costly to recreate high magnetic fields in a laboratory and maintain them for long periods of time. Therefore, the Lorentz force is simulated by a weight attached to the center of the filament, while the filament is heated by the according current. The mass m of the weight is chosen in such a way that the gravitational force F_g matches the Lorentz force F_L which would act on the straight section of the filament for a given heating current I_h and a magnetic field $B = 8\,\mathrm{T}$, which is the highest field strength the filaments could be exposed to in ITER. The derivation of the formula for the mass is given by

$$F_\mathrm{g} = F_\mathrm{L} \tag{3.1}$$

$$m \cdot g = I_\mathrm{h} \cdot l_\mathrm{str} \cdot B \tag{3.2}$$

$$m = \frac{l_\mathrm{str} \cdot B}{g} \cdot I_\mathrm{h}\,, \tag{3.3}$$

with $g = 9.81\,\frac{\mathrm{m}}{\mathrm{s}^2}$ being the gravitational acceleration in Munich [21], which is very close to the Max Planck Institute for Plasma Physics in Garching, the location of the laboratory in which the creep tests were carried out, and $l_\mathrm{str} = 1\,\mathrm{cm}$ the length of the straight section. To simulate the reversed force direction with the same approach, the filament has to be operated upside down.

It is shown in [14] that for ear filaments, the stresses in the filament created by the weight are similar to the stresses which occur for exposure to the according Lorentz force, even though the continuous force distribution of the Lorentz force is replaced by a force acting on a single point of the filament. This does not apply to the creep tests of meander filaments, as the evaluation in chapter 4 shows that the straight section of the filament bends at the attachment point of the weight. However, the creep tests are still suitable for simulation of the mechanical stress on a filament in a tokamak, since the weight tends to cause either similar, or more stress in the filament as it would experience under exposure to the according Lorentz force. Therefore, if a filament turns out to be stable in the creep test, it is expected that it will also perform well in a fusion device.

In the following, the implementation of this creep test concept is described. The filament is mounted on a holder, as shown in fig. (3.1). The base of this setup is formed by a stable bronze bridge attached to a 40 CF flange. Two copper bars are attached beneath the bridge using ceramic luster terminals, each of the bars leading to one fixation of the filament. Additionally, a stainless steel plate is placed on top of the bridge, which is used as an electrode for measurement of the electron emission of the filament. The bars and the electrode are connected to vacuum feedthroughs. The vacuum feedthroughs of the copper bars and the electrode are connected to a special multifunctional power supply of a custom design, which was previously used for operation of pressure gauges. This device is able to provide a heating current of up to 30 A while simultaneously holding the filament at a potential of 70 V. The same power supply also sets the electrode to a potential of 250 V to attract and collect the emitted electrons by imitating the acceleration grid potential inside a manometer, which is done to observe the emission behaviour of the filament. However, the potential in the experiment does not exactly match the potential inside a manometer, as the distance between the filament straight section and the electrode is always kept at 8 mm instead of 5 mm, which is the distance between a filament and the acceleration grid inside a manometer. The enlarged distance in the experiment was chosen to prevent contact of a deforming filament with the electrode.

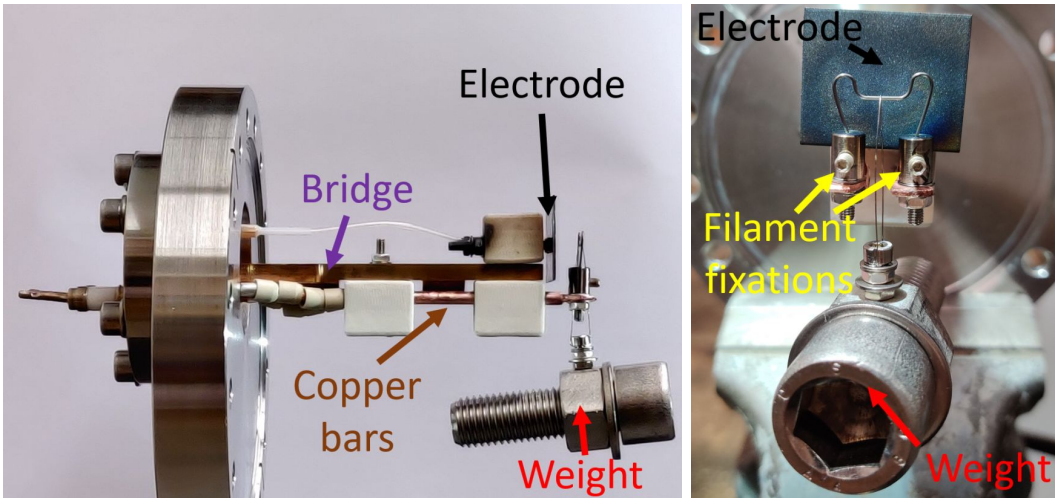

(a) Side view of the construction.

(b) Front view of the construction.

Figure 3.1: Images showing the central part of the experimental setup. (a) side view of the holder: The bridge supporting the copper bars below it and the electrode above, the flanges on which the bridge is mounted and the screw, which is attached to the filament to serve as a weight. (b) front view of the holder with the filament and the fixations, the screw, the thin tungsten wire connecting the weight to the filament and the electrode surface behind the filament.

The weight used to simulate the mechanical stress is made of a screw with screw nuts and washers, mainly because of its customizability, and the connection to the filament is made by a tungsten wire with a diameter in the range of $0.20 - 0.25$ mm. It is important to use thin wires for the connection to minimize its heat conductivity and thus, heat losses at the center of the filament during a creep test.

The 40 CF flange is decentrally mounted on a 100 CF flange which is connected to a vacuum chamber, closing the bridge and all mounted components. The chamber has only very limited space in vertical direction, which leads to the necessity of the two-flange system. This setup allows for the bridge to be as high as possible relative to the chamber walls to leave enough room for the weight, while also being rotatable at the same height, which is necessary to perform creep tests for both force directions.

In the chamber, a pressure in the range of 10^{-7} mbar to 10^{-6} mbar can be reached and maintained during a creep test using a turbo pump supported by a backing pump, which is necessary to prevent oxidation of the filament while it is heated.

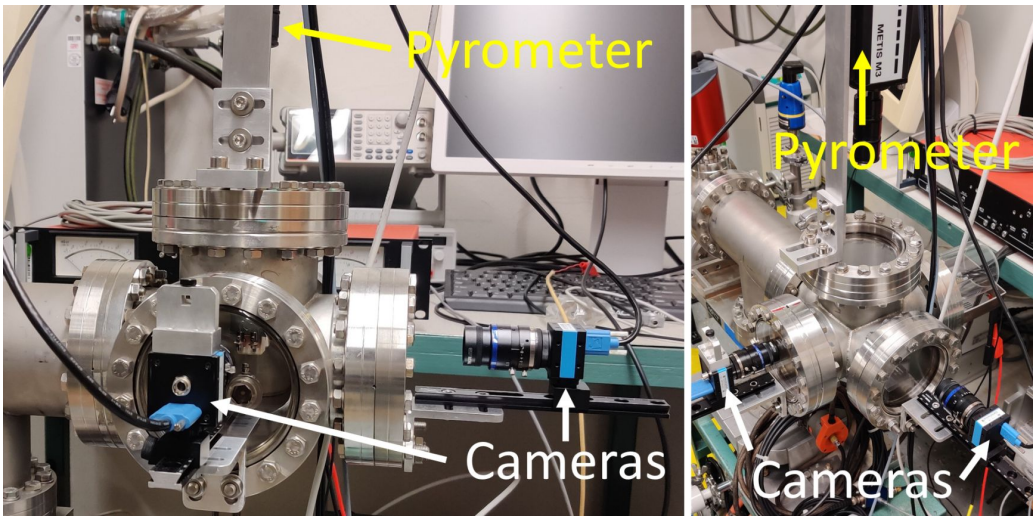

Figure 3.2: Photography of the full experimental setup, displaying the vacuum chamber, the vacuum windows and cameras positioned at the vacuum windows to record the front and side view of the filament.

The vacuum chamber has three vacuum windows, one in front, one at the side and one above the filament with each having a rail attached to its edging. Both lower rails each carry a monochrome camera to capture images of the front and side view of the filament. The camera recording the front perspective of the filament is a "DMK 37BUX264" camera from "The Imaging Source" with a resolution of 2448×2048 (5 Megapixel), a global shutter and a 16 bit output format. The camera for the side view is a "DMK 72AUC02" camera from "The Imaging Source" with a resolution of 2592×1944 (5 Megapixel), a rolling shutter and a 8 bit output format. The top rail holds a "Metis M313" pyrometer from "Sensortherm", as shown in fig. (3.2). The Metis M313 can measure the temperature at a wavelength of 1.27 µm in a circular area with the diameter of 0.3 mm. This wavelength was chosen as it corresponds to the point at which the temperature-dependent emissivity curves of tungsten intersect, which allows to set the emissivity ϵ to 0.33 for the temperature measurements [22]. The cameras take pictures of the heated filament, which are then processed further to extract information about the deformation. The filament can get very bright for heating currents above 15 A, which can easily lead to overexposure of the camera sensors. Therefore the cameras are equipped with $335 - 610$ nm bandpass filters to reduce the illumination intensity on the sensors, as the filament mostly radiates in the infrared wavelength region.

For the measurement of the electron signal, a 500 Ω shunt resistor is added in series to the electrode circuit. Additionally, a 2.0 mΩ shunt resistor is connected in series to the filament for the measurement of the heating current. The outputs of the shunts are passed through isolation amplifiers to get a signal relative to ground potential, and in the case of the 2.0 mΩ shunt, the signal also gets amplified by a factor of 100 to get a signal in the V range instead of 10 mV. This is done to make better use of the voltmeter measuring-range, which is −35 V to +35 V, as this improves the accuracy of the heating current measurement. A detailed list of the used components for the setup of the electronics is shown in tab. (**??**).

The majority of the setup is controlled by a python program running on a Raspberry Pi 4, which is a microcontroller. It controls both cameras, managing their settings and the camera trigger, and with the help of some additional electronic components from "Tinkerforge", it can also measure the signals from both shunts and activate or deactivate the power supply using a relay.

The general procedure of a creep test starts by taking three pictures of the front and the side of the filament while it is not heated, so that the fixations of the filament are clearly visible. These pictures are used to derive the relationship between distance in pixels and distance in millimeters at the level of the filament. After that, the camera settings are optimized for a heated filament and the experiment starts as the power supply gets activated by the relay. While the filament is heated, the cameras continuously take pictures every 8 s to 15 min, depending on the expected duration of the experiment. At the same time, the measured signals from the shunts are written into a text file. The frames are saved in a TIFF-format to keep the bit-depth of the pictures made by the DMK 37BUX264 camera at 16 bit. All images and text files are simultaneously copied to the institute servers to secure the data and then, the images are deleted from the microcontroller to prevent reaching its maximum storage limit. The creep test runs until the distorted filament shape clearly exceeds the deformation tolerance allowed inside a manometer. At this point, the experiment is shut down manually.

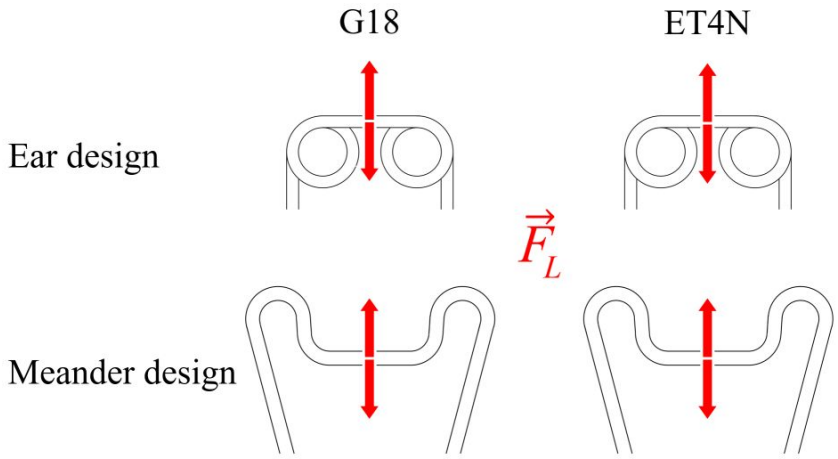

Figure 3.3: Schematic showing all tested configurations of filament design, material and force direction.

Each filament shape was tested with the G18 and the ET4N material while always considering both force directions, which adds up to eight measurements in total, as shown in fig. (3.3). All ear filaments were tested with a heating current of 17 A and a weight of approximately 140 g, which results from eq. (3.3), and the meander filaments with 18 A and a weight of about 150 g. The heating currents used for the creep tests were set to those values to achieve the same central temperature for both filament shapes, as explained in the following section.

Chapter 4

Evaluation and comparison of filament creep resistance

In this chapter, important aspects of the experiment evaluation are discussed. First, the determination of the heating currents for the ear and meander filament creep tests is shown, followed by an explanation of the image processing, which is used for the evaluation of the creep tests. After that, the results of the creep tests are presented, followed by a theoretical determination of the impact of filament wire diameter on its stability.

4.1 Determination of the heating current settings for filament creep tests

Before the start of the creep tests, two experiments had to be carried out in order to determine the heating current settings for the ear and the meander filament creep tests. The idea was to find a suitable setting for one of the filament designs first and then to set the heating current for the other filament design in such a way that the electron emission levels from the straight filament sections of both designs are equal, which is necessary to make the creep tests comparable to each other.

Since the heating current of a filament is constantly regulated by the feedback loop during manometer operation to ensure a stable electron flux in the manometer, there is no typical heating current for filaments which could have been used for the creep tests. Using the feedback loop for the creep tests is also not an option, since it would make the creep tests not comparable to each other. It could be observed, that the measured electron signal at the electrode depends on the pressure inside the chamber. When the filament is first heated, the pressure can change in an unpredictable way to some extend, as the sudden increase of the filament temperature may cause some particles to dissolve from the surfaces inside the vacuum chamber. This would also have an unpredictable impact on the measured electron signal at the electrode and thus, the heating current, if the filament was operated with an active feedback loop. Since the pressure only changes very slowly at pressures below 10^{-5} mbar, which usually is the pressure range in which the pressure fluctuates during the start of the measurement, this effect can not be compensated quickly and may impact the whole measurement. This would make creep tests with an active feedback loop incomparable to each other.

Since there is no typical heating current value for the filaments, a different approach is used to determine a suitable heating current. It could be observed in unrelated experiments that sometimes a heating current of 15 A was already sufficient for manometer operation. Therefore, the idea was to observe the emission behaviour of a filament for different heating currents to determine a heating current with the criteria, that the emission level for the chosen heating current has to be clearly higher than the electron emission at a heating current of 15 A. This criterion is chosen since it favors a higher load in the creep test compared to the mechanical stress inside a tokamak rather than the other way around. This is the better of the two options, since in such case, a filament showing a good creep resistance in the creep test can also be expected to perform well inside a tokamak.

Once the heating current of one filament design is known, the heating current of the other filament design is determined using the criterion, that the electron emission levels of both filament straight sections have to be equal. Since the electrode in the setup does detect electrons emitted from the whole filament and not only from the straight section, the measured electron signal cannot be used for the implementation of this approach. Instead, the temperature of the straight section center of both filaments is matched, since equal temperatures in the wire have to lead to a similar emission behaviour of the filaments for the same material.

4.1.1 Identification of the heating current setting for meander filaments

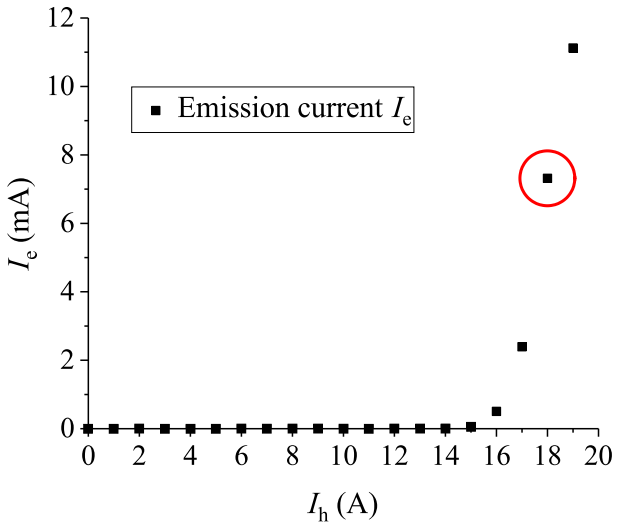

Figure 4.1: Measured electron signal of a G18 meander filament for a gradually increasing heating current. Strong rise of the electron signal at a heating current of 18 A (circled in red).

As an implementation of the previously described approach to determine a suitable heating current, a G18 meander filament was inserted into the setup without any weight attached to it and was first heated for about 17 h by a heating current of 20 A. This was done to stabilize the electron emission of the filament, since the electron signal was observed to

change drastically in the first hours of heating. After this commissioning of the filament, the heating current was lowered to 0 A and then increased in 1 A steps to observe the emission response of the filament. The results are shown in fig. (4.1).

It can be seen that the measured electron emission current stays at 0 A for heating currents up to 14 A. At 15 A, the first small response can be seen and for higher currents, the measured emission increases steeply.

The main objective of this measurement was to determine the heating current which will be used for the creep test of meander filaments with the main decision criterion being an electron emission clearly higher than the electron emission at 15 A. This was given for a heating current of 18 A, which was therefore chosen for the creep tests of meander filaments.

4.1.2 Identification of the heating current setting for ear filaments

To determine the heating current for ear filament creep tests, a G18 ear filament was mounted to the bridge without a weight. A pyrometer was fixed to the top rail of the setup and was adjusted until it focused on the center of the filament. Then, the filament was heated with a current of 20 A until the temperature stabilized. After that, the heating current was reduced in 1 A steps while noting the temperature of the filament until the pyrometer did no longer receive enough radiation to measure the temperature. The same experiment was repeated for a G18 meander filament. The results are shown in fig. (4.2).

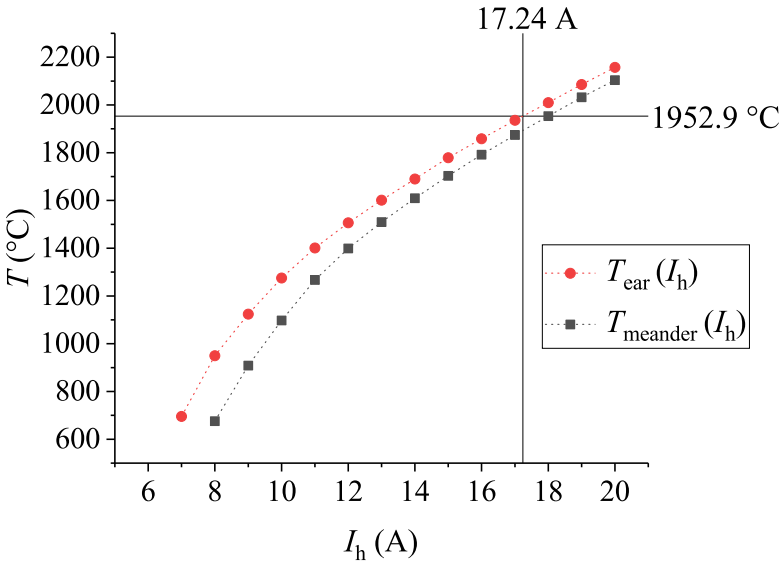

Figure 4.2: G18 Ear and meander filament temperature (T_{ear}, T_{meander}) depending on the heating current. Meander filament temperature level at 1952.9 °C for a heating current of 18 A and according heating current of 17.24 A to reach the same temperature in the center of an ear filament.

It can be seen that for both filaments, the temperature response shows a linear dependence for high currents. For lower temperatures, however, the curve is not linear, indicating that the decrease in temperature is higher for a given reduction of current.

The curves have an approximately constant temperature offset relative to each other, which results from the difference in filament wire length.

To determine the appropriate heating current for the ear filaments, a horizontal line is added at the temperature level of the meander filament for a heating current of 18 A, as its intersection with the ear filament curve shows at which heating current the same temperature was reached in the ear filament. As can be seen in fig. (4.2), the intersection leads to a heating current of about 17.24 A. However, a heating current of 17 A was chosen for the creep test, due to an additional observation made in the experiment: During the adjustment of the pyrometer for the measurement, it sometimes focused on areas on the outer regions of the filament straight sections. It could be observed that for the ear filaments, the outer regions are at a slightly higher temperature than its center, which is most likely related to the spirals. For meander filaments, no such behaviour was noticed during pyrometer adjustment, therefore the center is expected to be the hottest region. Consequently, to better match the temperature levels of the whole filament straight sections, the heating current of the ear filament was lowered to 17 A.

It has to be mentioned that the pyrometer had a tendency to be more inaccurate for lower filament temperatures, as the measured temperature would not fully stabilize at one value. However, this did only occur outside the linear dependency region, therefore at least the data from heating currents above 13 A should be reliable. There are no data points below 7 A since the pyrometer could not pick up enough radiation to measure the temperature.

4.2 Image processing for creep tests

During a creep test, the deformation of the filament is recorded from a front and side perspective. The frames of these recordings constitute the main raw data obtained from the experiment. In this section, the evaluation principle of the filament pictures is explained.

4.2.1 Image calibration

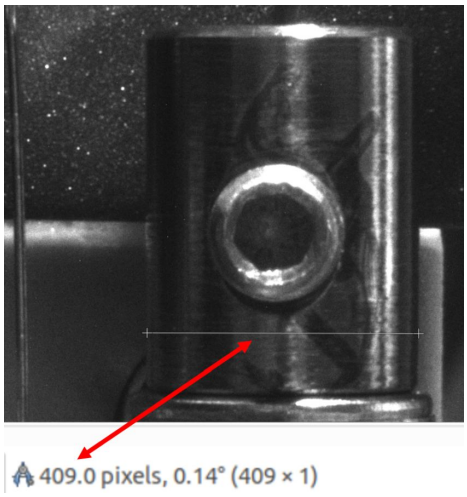

Figure 4.3: Picture of the filament fixation width measurement with GIMP, showing the cursors and the respective pixel distance determined by the program.

The first step of the evaluation is to determine the relationship between the number of pixels and the according distance in mm in the layer of the filament. For that, the calibration images are used, in which the filament is not heated and therefore the surroundings are visible. The filament fixations are used as reference objects, as they have a cylindrical shape with a known diameter of 6 mm. The fixation width in the image is measured using GIMP, since this program has a feature which can tell the distance in pixels between two points marked on the image, as shown in fig. (4.3). To reduce the error of the calibration, the measurement is performed for three pictures and the results are then averaged. This is done for each perspective separately.

A typical value of the average fixation width for the front view is 408.9 pixels. The standard deviation from the average fixation width is normally below 1 pixel. Even if an error of 1 pixel is used, the conversion of distances in pixels y_p into distances in millimeter y_mm results in

$$y_\mathrm{mm} = \frac{6\,\mathrm{mm}}{408.9} \cdot y_\mathrm{p} = (14.67 \pm 0.04) \cdot 10^{-3}\,\mathrm{mm} \cdot y_\mathrm{p}\,, \tag{4.1}$$

whereby the error of the conversion value resulted from the gaussian error propagation. It can be seen that the uncertainty of the conversion value is only in the fourth digit. This shows that using three calibration pictures is sufficient for an accurate calibration.

4.2.2 Filament tracking technique

Once the calibration is finished, the recordings are evaluated by a dedicated image analysis algorithm implemented in Python, which I have developed for this thesis. The general functionality of the algorithm is described in the following.

The frames are read in using the "tifffile" library. The first step of the algorithm is a preparation of the images which mainly removes reflections on the components of the setup from the image. For that, the program divides all pixels in the image into two different categories. One category is dark pixels, which are pixels with a brightness smaller than a certain percentage of the maximum possible brightness. These pixels resemble the background in the picture. All pixels falling into this category are set to a brightness value of 0, which turned out to be helpful for later steps of the algorithm. The other category are bright pixels, which are pixels with a brightness higher than the given percentage of the maximum possible brightness. These pixels resemble the glowing sections of the filament. The percentages used for the program were set to 10 % for ear filaments and 20 % for the meander filaments, as these settings turned out to work the best for the program. The program then searches for groups of pixels, which are connected pixels of one category. If the number of pixels in the group is smaller than a user defined threshold, the brightness of the pixels is set to 0 when it is a group of white pixels, or to the average of the pixel brightness of the group-surrounding pixels when it is a group of white pixels. After this preparation of the images, different algorithms are applied depending on the filament design and the perspective being analyzed.

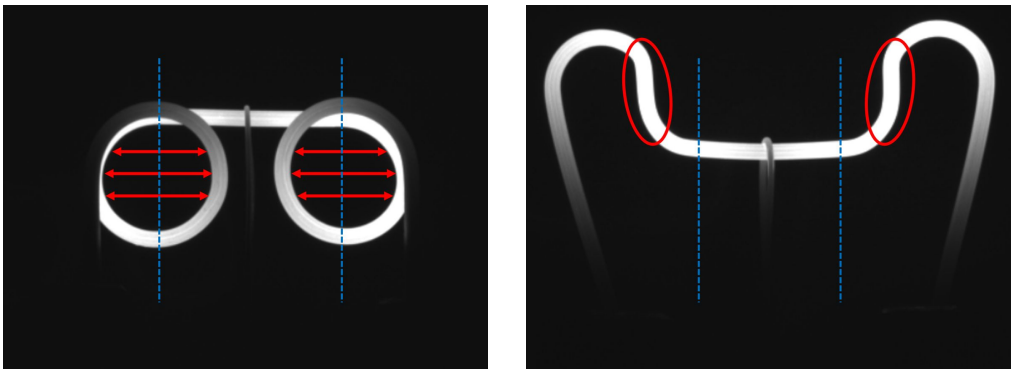

(a) Determination of the straight section region of an ear filament.

(b) Determination of the straight section region of a meander filament.

Figure 4.4: Images visualizing the programs approach for determining the horizontal region, in which the filament straight section can be found. The filament areas which are used as a reference for the determination are marked in red and the horizontal region borders in blue. (a) shows the process for an ear filament, where the average center in each spiral defines the border location, and (b) for a meander filament, where the borders are placed at a certain distance away from the arc transitions.

For the front view, the program first determines the left and right boundary in horizontal dimension, in which the straight section of the filament is tracked later. If it is analyzing images of an ear filament, it uses the spirals to define the boundaries. Using the

previously discussed categorization of pixel brightness, the program can find the spirals of the ear filaments in the picture. The spirals are the only regions in the picture, were dark pixel groups are fully surrounded by bright pixels. Once the spirals are found, the program goes through each line of the picture region where the spiral is located. For each line, it searches for the left-most and right-most point of the dark pixel group, which is surrounded by the spiral. From the left-most and right-most point, the algorithm calculates the center of each dark pixel group line. At the end, the calculated center positions of each line are averaged, which results in a coordinate resembling the horizontal position of the spiral center. The horizontal coordinates of each spiral center are used as the left and right boundary in horizontal dimension, in which the straight section of the filament is tracked, since at those positions, the straight section starts to transition into the spirals. The general working principle of this part of the algorithm is illustrated in fig. (4.4a).

For the meander filament, first, the left-most and right-most point of the filament is determined. From that, the horizontal position of the filament center is calculated. Then, the program searches the highest point of the filament for the left and the right half of the filament. These two points resemble the highest point of each arc in the filament. After that, the program goes through each column of the image between the horizontal coordinate of the arc and the filament center. It searches for the column with the highest number of bright pixels, which then defines the horizontal coordinate of the transition from the arc of the filament to the straight section. It is important to limit this search between the horizontal coordinate of the highest point of the arc and the filament center, since otherwise the program could erroneously define the outer regions of the filament as the transitions from the arc to the straight section. After the horizontal coordinates of the transitions from the arc to the straight section are found, the distance between them is calculated. The distance is divided by four and then rounded to an integer. Finally, this result is added on the horizontal position of the left arc and subtracted from the position of the right arc. The resulting coordinates are defined as the left and right boundary in horizontal dimension, in which the straight section of the filament is tracked. The general working principle of this part of the algorithm is illustrated in fig. (4.4b).

The distance between the left and right boundary is the half of the distance between the horizontal coordinate of the left and right transition from the arc to the straight section. This proportion was chosen since during the creep tests, the straight section of meander filaments sometimes bent at the attachment point of the mass, which causes the arcs of the filament to get closer to each other. It had to be made sure that the actual horizontal region in which the straight section of the filament can be found does not get smaller than the measurement region.

At this point of the analysis, the actual tracking of the filament straight section starts. The general idea of the tracking process is the generation of a shape resembling the straight section of the filament, followed by a rating of the shape with a score, based on how well it fits the image. The shape is continuously adjusted until the score is maximized. When the program finished the evaluation of one frame and continues with the next, it uses the previously adjusted shape as a basis for the current frame. For the first image of the evaluation, it starts with a rectangular shape, since the filament should not have yet been deformed significantly.

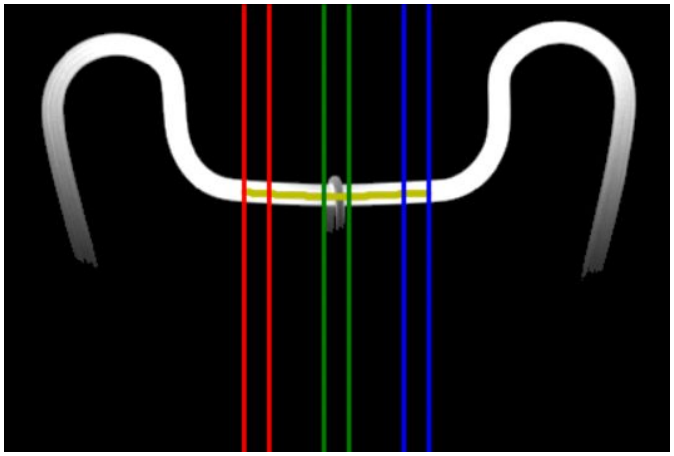

Figure 4.5: Illustration of the analysis algorithm working principle. The line, resulting from averaging the lower and upper border of the fitting shape is shown in yellow. The left-hand region, in which the vertical positions of the points in the yellow line are averaged is shown in red, the central region in green and the right-hand region in blue.

When the best fitting shape for one frame is found, the program calculates the average between the lower and upper border of the shape, which results in a line, as can be seen in fig. (4.5). The vertical coordinates of the points in the line are then averaged at the left center and right. The regions, in which the vertical positions are averaged, have a horizontal width of 50. These measurement regions are also shown in fig. (4.5).

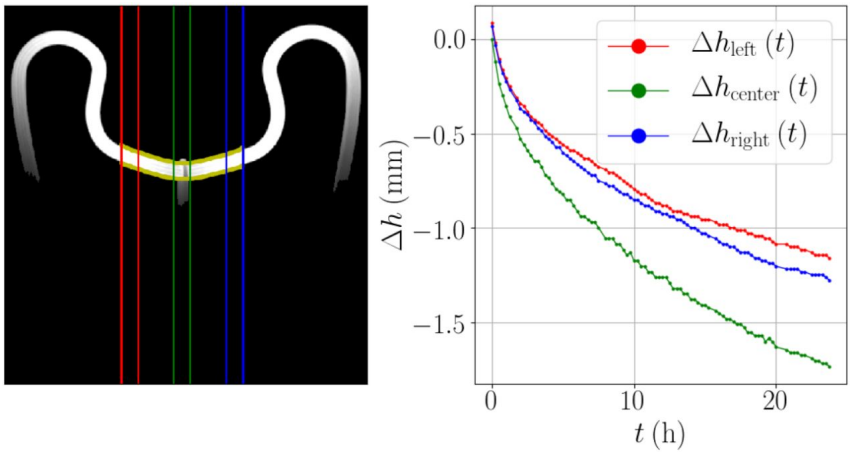

Figure 4.6: Example video frame of a meander filament front view evaluation for a downwards force direction, created by the program for verification of the evaluation process. On the left, the images of the deforming filament are shown with the red, green and blue column marking the area in which the average position of the straight filament section is calculated and the yellow lines showing the tracking of the filament straight section by the program. The right-hand side shows the temporal evolution of the height change, with the red, green and blue curve representing the height change of the filament straight section in the respective column shown on the left.

After that, each vertical coordinate is subtracted from the vertical coordinate of the center in the first image of the measurement, the difference of these points therefore represents the deviation of the filament straight section from its original position. This difference is converted to a unit of mm using the conversion determined in the calibration and then written into a text file. Additionally, the program creates a video showing each frame of the experiment, the shape which the program fitted to the image, the measurement positions and the development of the height change over time plot. This is done to ensure that the evaluation performed correctly. An example frame of such a video is shown in fig. (4.6) for the evaluation of a meander filament creep test with a downwards force direction.

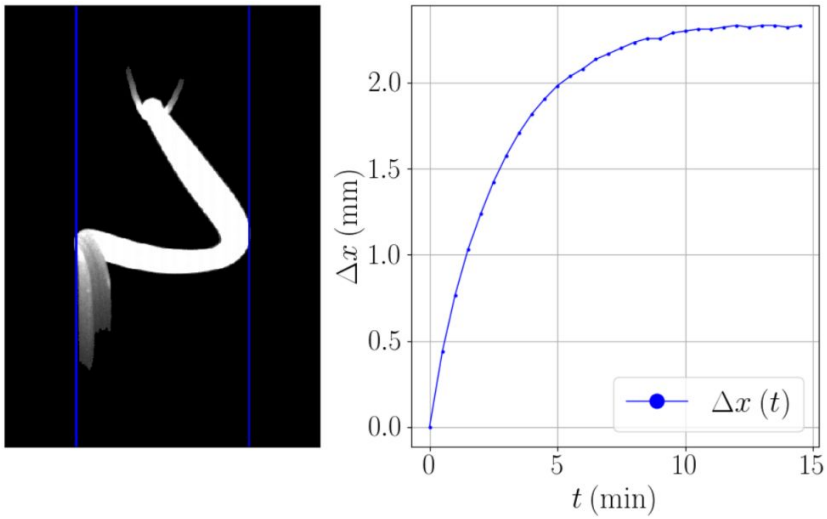

Figure 4.7: Example video frame of an ear side view evaluation with an upwards force direction, created by the program for verification of the evaluation process. On the left, the images of the deforming filament are shown with the blue lines marking the left-most and right-most point of the filament. The right side shows the temporal evolution of the width-change, which is the difference between the right-most and left-most point of the filament.

The evaluation of the side perspective uses a much simpler approach, since there is no trackable object such as the straight section in the front perspective. Thus, the evaluation idea is to simply record the left-most and right-most point of the filament. The subtraction of their horizontal coordinates represents the width change of the filament, which is also converted to the unit of mm and written into a text file. As in the evaluation of the front view, the program also generates a video showing the evaluation process of the side perspective, marking the left-most and right most-point in the frames and showing the development of the width-change over time plot. An example frame of such a video is shown in fig. (4.7) for the evaluation of an ear filament creep test with an upwards force direction.

4.3 Determination of filament stability in creep tests

In this section, all important aspects of the creep test results are shown and discussed. First, the filaments are ranked based on their resistance to creep processes and afterwards, noteworthy observations during the creep tests are presented and discussed. The full evaluation of each individual creep test is presented in appendix A.

The filament performances are compared to each other by determining the time t_d required to reach a 1 mm deviation of the filament straight section from its original position. This is the maximum deformation tolerance inside a manometer, since at this point, a significant portion of the emitted electrons will hit the control electrode, leading to an increase of the heating current due to the feedback loop, as was described in section 2.3. Since the filament straight section did not always keep its shape during a creep test, the comparison was done using the first point reaching the 1 mm threshold. The best combination of filament design, material and force direction was the meander filament with a downwards force direction, since this configuration required the longest time to reach the threshold. The ranking can be seen in tab. (4.1). Additionally, tab. (4.1) includes the deformation time for a 4 mm deviation to show the further development of the deformation processes.

Table 4.1: Ranking of the creep resistance for all combinations of filament shape, material and force direction, sorted after the deformation time t_d for a 1 mm height change.

Design	**Material**	**Force direction**	t_d **(1 mm)**	t_d **(4 mm)**
Meander	ET4N	down	7.5 h	8.0 d
Meander	G18	down	49.5 min	16.7 h
Meander	ET4N	up	20.8 min	23.6 min
Meander	G18	up	16.8 min	40.0 min
Ear	ET4N	up	2.4 min	13.8 min
Ear	G18	up	28 s	5.5 min
Ear	ET4N	down	16 s	1.6 min
Ear	G18	down	14 s	3.2 min

From the ranking shown in tab. (4.1), a few different tendencies can be deduced. One outcome was that all of the meander filaments performed better than the ear filaments, regardless of material or force direction. All ET4N filaments performed better than their G18 counterparts for the deformation threshold of 1 mm, but in most cases only to a small degree. No general dependency on the wire material could be found for the 4 mm deformation threshold. For the best configuration, which is the meander filament with a downwards force direction, the ET4N wire performed significantly better with a deformation time of t_d (1 mm) = 7.5 h, which is by a factor of 9 larger than its G18 counterpart with a deformation time of t_d (1 mm) = 49.5 min. Another noteworthy tendency is that

the creep resistance of ear filaments is better for an upwards force direction than for a downwards force direction and for meander filaments it is the other way around.

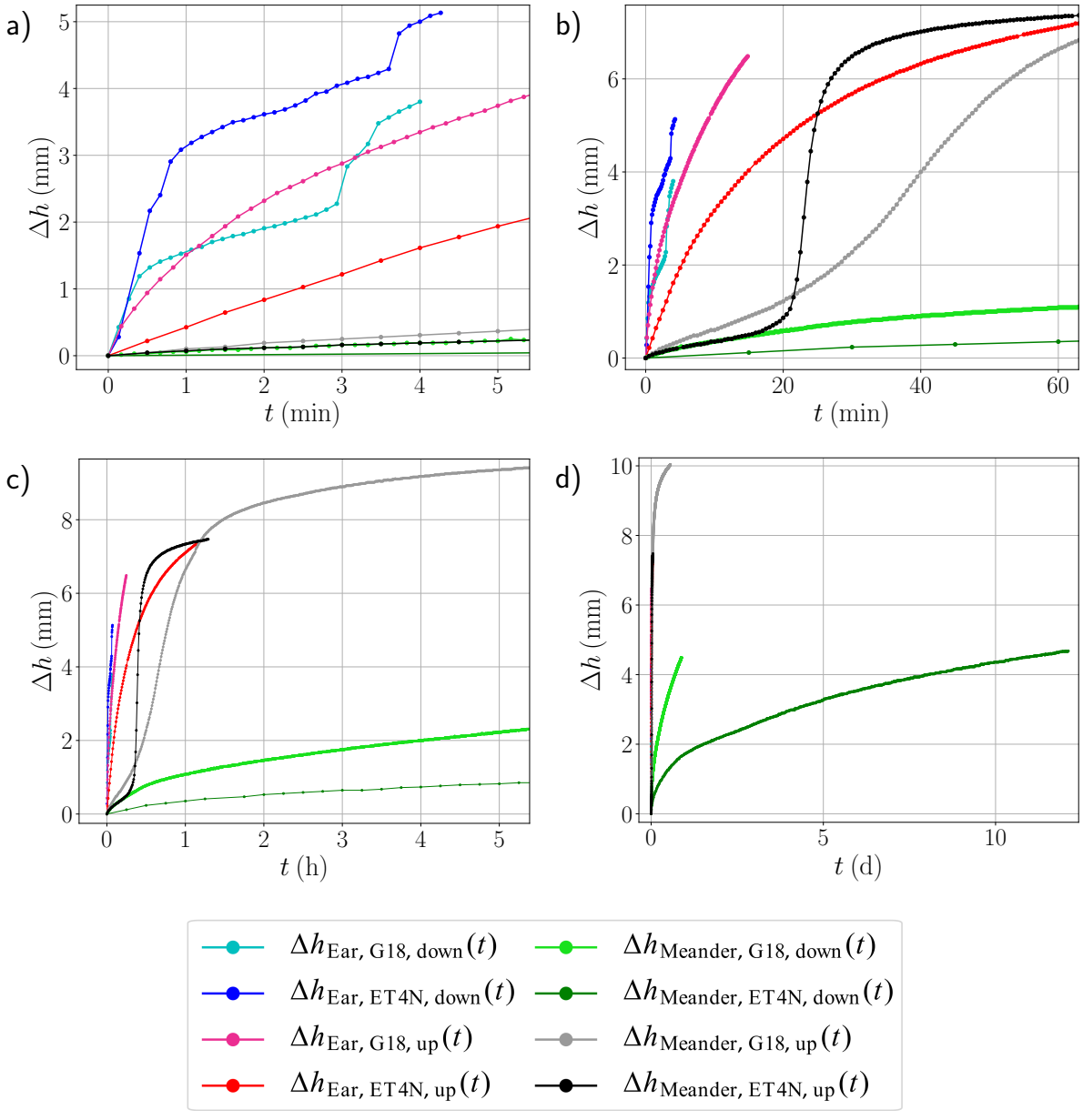

Figure 4.8: Comparison of all filament creep test evaluations, showing the temporal development of the absolute value of the height change in the center of each filament. (a) shows the first 5 minutes of all creep tests, (b) the first hour, (c) the first five hours and (d) the full temporal development of all measurements.

Some of these observations can be explained by examining the stresses acting on the filament shapes for given force directions with the help of fig. (4.8), where all deformation processes are shown. The ear filaments always experience a torque from the Lorentz force induced by a homogeneous magnetic field, which is a consequence of their 3D structure. The meander filaments can also experience torque for an upwards force direction, as shown

in fig. (4.9). The major problem of the torque is that it causes the filaments to "unfold", which in some cases reinforces the torque further. The reinforcement occurs when a section of the filament is representing a lever and is oriented increasingly perpendicular to the Lorentz force as the filament deforms. This cycle causes the filaments to fail quickly once a torque starts acting on them. The torque reinforcement cycle can be seen most clearly in fig. (4.8b) for meander filaments with an upwards force direction.

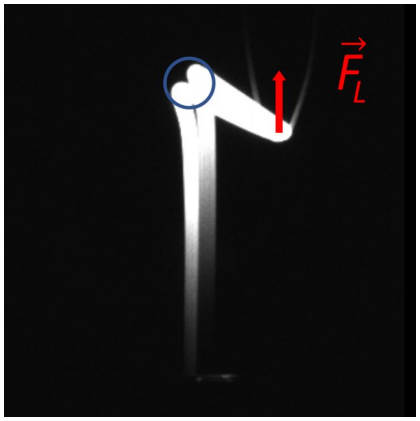

Figure 4.9: Side view of a meander filament exposed to an upwards force direction, showing the unfolding of the filament which causes torsion stresses on the arcs of the filament. The affected regions are marked blue and the simulated Lorentz force in red.

Since the meander filament has a planar shape, there is initially no significant torque acting on the filament. However, this situation is unstable, as once the filament straight section moves out of the plane, even if only to a very small degree, it leads to torque acting on the arcs of the meander filament, causing the filament to unfold as shown in fig. (4.9) and thus leading to a torque reinforcement cycle. It can be seen in fig. (4.8b) that the deformation rate of the meander filaments is slow at the beginning of the measurement and starts to increase rapidly at about 20 min. At this point, the straight section of the filament moved out of the plane enough to start the torque reinforcement cycle. The deformation continues until a height change between 3.5 mm to 4 mm is reached, at which the torque reinforcement cycle ends, since the lever section of the filament is perpendicular to the force and therefore the torque is at its maximum. After this point is reached in the deformation process, the deformation starts to decrease again, as the lever section of the filament gets increasingly parallel to the force. Once the lever section of the filament is mostly parallel to the force, the deformation slows down to a similar rate as in the beginning of the measurement. The ear filament experiences the torque reinforcement cycle for a downwards force direction. It can be seen in fig. (4.10b) that the lower region of the spiral experiences major torque, as the transition from the spirals to the straight section of the filament represents the lever section of the filament. Therefore, a similar deformation behaviour as for the meander filaments with an upwards force direction is expected. However, the torque reinforcement cycle was interrupted by the occurrence of a short circuit in one of the spirals. The short circuit reduced the filament resistance and thus, its heating and therefore the deformation rate. When the contact worsened, the deformation rate increased again. This leads to the step-like temporal development of the ear filament deformation for downwards force direction, which can be seen in fig. (4.8a).

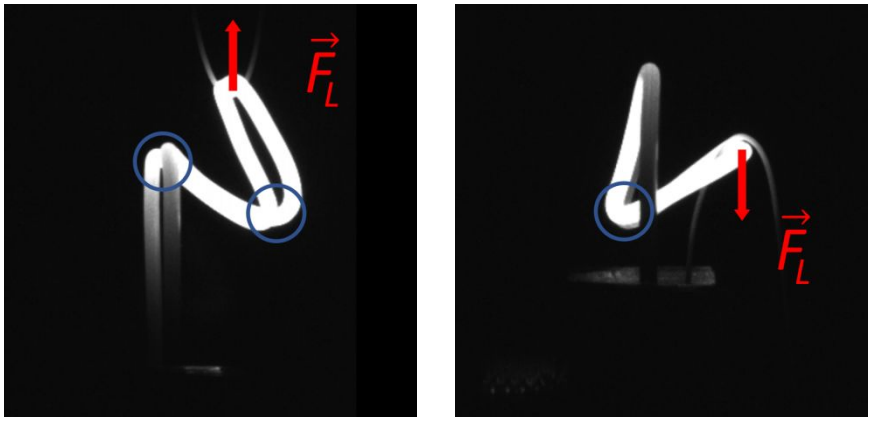

(a) Upwards force direction. (b) Downwards force direction.

Figure 4.10: Unfolding process of ear filaments shown for (a) a upwards and (b) an downwards force direction. The filament regions experiencing the major torque are marked in blue and the applied force direction in red.

The ear filament does also unfold for an upwards force direction, as can be seen in fig. (4.10a). However, the torque reinforcement cycle did not occur for this configuration, as can be seen in fig. (4.8a). This is most likely due to the fact that for the upwards-facing force, the whole spiral is pulled apart, leading to two regions of each spiral experiencing a torsion stress. Consequently, the stress is distributed to two points of the spiral. This leads to a more complicated deformation process, which cannot be described with the torque reinforcement cycle.

The distribution of the stress to two points of the spiral most likely also explains the observation of a better stability of ear filaments with an upwards force direction compared to the ear filaments with a downwards force direction, visible in tab. (4.1). The main reason explaining the higher creep resistance of meander filaments with an upwards force direction compared to the ear filaments is that the planar shape delays the start of torque reinforcement cycle, since the cycle only starts once the filament deviated from its planar shape. Therefore, the deformation rate of the meander filaments is slow in the first minutes, while the deformation rate of the ear filaments is at its highest at the start, as can be seen in fig. (4.8b), which leads to the better performance of meander filaments with upwards force direction compared to ear filaments.

The only shape and force direction which do not suffer from torque reinforcement cycles are meander filaments with a downwards force direction. For this configuration, the filaments stay planar for the whole measurement, as can be seen in fig. (4.11). This explains the observation that the meander filaments with a downwards force direction stand out significantly in terms of their creep resistance.

When examining the difference in creep resistance for the G18 and ET4N wires, it can be seen that the deformation time t_d (1 mm) of the ET4N filaments was higher, but in most cases only to a small degree. However, some of the G18 filaments performed better for the 4 mm threshold. Only for meander filaments with a downwards force direction, the ET4N filament showed a by far superior creep resistance to the G18 filament. This was also the configuration where no significant torsion stresses appeared during deformation.

The comparison of the filament creep resistance for the G18 and ET4N material therefore leads to the conclusion that the non-sag property of ET4N is very effective if no torsion stresses are involved.

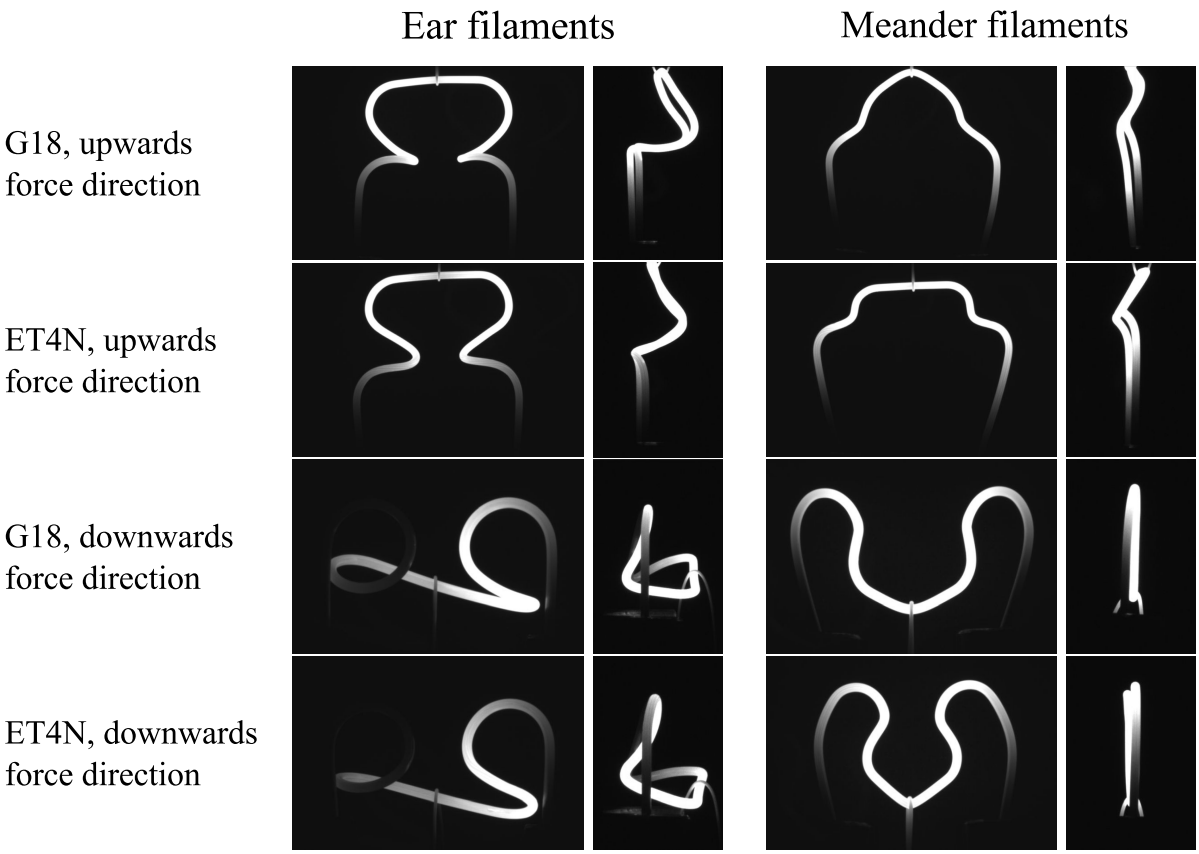

Figure 4.11: Final frame of the front and side view for all creep tests.

Apart from the ranking of the filaments, another surprising observation could be made during the evaluation of the creep tests. When comparing the deformation process of G18 and ET4N filaments with equal shape and force direction, the process was usually similar, with the only difference being the duration of the deformation process. This can be seen in fig. (4.11), where the final frames of the front and side view is shown for all creep tests. The meander filaments with an upwards force direction show a small difference in their straight section, but the major deformation process, which was the unfolding of the filament, was similar for both creep tests.

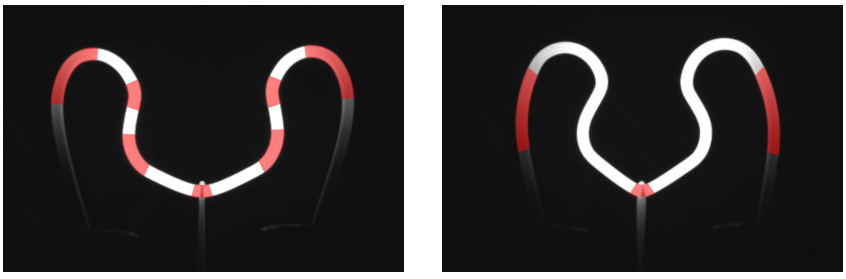

(a) Final deformed shape of the G18 meander filament.

(b) Final deformed shape of the ET4N meander filament.

Figure 4.12: Deformed shape of (a) the G18 and (b) the ET4N meander filament at the 4 mm deformation threshold, with the most deformed regions marked in red.

However, the deformation processes of meander filaments with a downwards force direction were not as similar, it could be observed that different regions suffered more from deformation, depending on the filament material. This can be seen in fig. (4.12), where the deformed shapes of the G18 and ET4N meander filament at the 4 mm deformation threshold are shown and the most deformed regions of each filament are marked.

The central region of the G18 filament, reaching from one arc to the other, deformed the most, which was expected since this region is at higher temperatures than the sides of the filament. It can be seen that the arcs of the filament lost their original shape and the region between the straight section and the arcs was straightened to some extend. For the ET4N filament, however, the arcs and the transitions between the arcs and the straight section were only deformed slightly. Instead, the sides of the filament curved inwards far more than it is the case for the G18 filament. This is surprising, as the outer filament regions are at a lower temperature and are therefore expected to be more robust than the filament center which is at a very high temperature. It is speculated that these deviations in the deformation process might be caused by a different reaction of the materials to the manufacturing (=bending) of the filament. This idea is based on the observation that the arcs and the transitions to the straight region of the filament are those areas which had to be bent during filament manufacturing to form the meander shape from an initially straight wire. These are also the regions which mostly kept their shape in the ET4N filament, which raises the assumption that the bending of the ET4N wire might have caused some structural changes in those regions, making them more resistant to creep processes than the other regions in the wire.

4.4 Impact of wire diameter on the creep resistance of filaments

To complete the evaluation of the filament stability, the impact of the wire diameter on the resistance to creep processes is discussed. The objective is to make an estimation, whether an increase of filament wire diameter will improve or worsen the filament stability. To estimate the impact of the wire diameter, changes in wire stability and heating current are taken into account. It is important to consider changes in the heating current, since it is proportional to the Lorentz force acting on the filament.

The forces acting on a wire usually scale with $1/A$, where $A = 0.25\pi \cdot d^2$ is the cross-sectional area of the wire and d the wire diameter. This would translate to a d^2 improvement of the wire strength. In ref. [18], an even stronger dependency of d^3 is expected for the wire strength. The impact of the wire diameter on the heating current is derived in the following.

The filament heating can be described by the formula for resistive heating

$$\dot{Q} = R \cdot I_\mathrm{h}^2 \tag{4.2}$$

with $\dot{Q}$ being the heat input per unit time, R the wire resistance and I_h the heating current. The resistance of the wire is given by

$$R = \rho \cdot \frac{l}{A} = \rho \cdot \frac{4l}{\pi \cdot d^2} \tag{4.3}$$

where ρ is the specific resistance, which is a material constant and l the wire length. The condition under which the wire diameters are compared is an equal temperature distribution in the filament, as this corresponds to a comparable electron emission behaviour of the filament surfaces. This condition can be translated to a requirement of a constant heating $\mathrm{d}\dot{Q}$ per wire surface area $\mathrm{d}S = \pi \cdot d \cdot \mathrm{d}l$ when assuming that the heat dissipation to the sides of the filament does not change significantly. The requirement of a constant heating per wire surface can be written as

$$\frac{\mathrm{d}\dot{Q}}{\mathrm{d}S} = \text{const.} \overset{4.2}{=} \frac{I_\mathrm{h}^2}{\pi \cdot d} \cdot \frac{\mathrm{d}R}{\mathrm{d}l} \overset{4.3}{=} \frac{4\rho \cdot I_\mathrm{h}^2}{\pi^2 \cdot d^3}\,. \tag{4.4}$$

Rearranging eq. (4.4) results in a $d^{\frac{3}{2}}$ dependency

$$I_\mathrm{h} = \frac{\pi}{2} \cdot \sqrt{\frac{1}{\rho} \cdot \frac{\mathrm{d}\dot{Q}}{\mathrm{d}S}} \cdot d^{\frac{3}{2}} \tag{4.5}$$

of the heating current, which is necessary to deliver a constant heat flux through the wire surface for a given wire diameter. Using eq. (4.5), the Lorentz force F_L acting on the straight section of the filament with the length l_str for a given magnetic field B can be calculated to

$$F_\mathrm{L} = \frac{\pi}{2} \cdot l_\mathrm{str} \cdot B \cdot \sqrt{\frac{1}{\rho} \cdot \frac{\mathrm{d}\dot{Q}}{\mathrm{d}S}} \cdot d^{\frac{3}{2}}\,. \tag{4.6}$$

The stability of the filament is therefore expected to improve at least with a $d^{\frac{1}{2}}$ dependency, since the wire strength is expected to improve at least with d^2, while the Lorentz

force rises only with $d^{\frac{3}{2}}$. For the wire strength improvement of d^3 which is expected in ref. [18], the stability of the filament increases with a $d^{\frac{3}{2}}$ dependency.

It has to be mentioned that eq. (4.5) is only an approximation, since the wire resistance also depends on its temperature, which is not considered in this derivation. Also, the heat dissipation to the sides of the filament was assumed to be constant, which might not be entirely accurate. Another important aspect is that demanding a constant heating per wire surface area does not correspond to an equal electron emission, since a larger surface area improves the emission for constant $\mathrm{d}\dot{Q}/\mathrm{d}S$. Consequently, if the filaments are compared at an equal electron emission, the heating current should actually be slightly smaller than the value given by eq. (4.5) for increasing wire diameters, which leads to a smaller Lorentz force than expected. This further supports the expectation of an improved filament stability for larger wire diameters. However, the highest inaccuracy of the derivation comes from the estimation of the wire stability, as the consideration of the force scaling does not include the filament shapes. Additionally, changes in the microscopical structure of the wires due to the change in diameter are not considered.

The calculation leads to the conclusion, that an increase in wire diameter is expected to improve the filament stability. This offers a route to a comparably simple modification towards a more robust setup.

Chapter 5

Summary and conclusion

In this study, we investigated the long term stability of hot cathode ionization manometers with a linear cathode arrangement. The filament of this type of manometer has to be orientated perpendicularly to the magnetic field, which can reach up to 8 T in ITER. This leads to strong mechanical stresses on the filament due to the Lorentz force. Combined with the high temperatures of the filament, these stresses lead to a deformation of the filament due to creep processes, eventually causing a manometer malfunction, which was investigated in detail in dedicated laboratory tests.

In these experiments, the Lorentz force was simulated by a weight attached to the center of the filament, whereby the mass is chosen in such a way that the gravitational force matches the Lorentz force which would act on the straight section of the filament. The creep tests were performed for the ear and meander filament design. Each design was tested for both force directions and for two different materials, G18, which is tungsten doped with 1.8 % ThO_2, and ET4N, which is tungsten doped with 0.4 % ThO_2 and 70 ppm potassium. The addition of potassium to the tungsten wire gives it a non-sag property, meaning a higher resistance to creep processes.

The main observations were that all ear filaments performed worse than any of the meander filaments. The meander filaments with a downwards force direction showed a by far superior resistance to creep processes. This configuration prevents the occurrence of torque, which was a major advantage to the other configurations, since the torque led to an unfolding of the filaments, which in some cases reinforced the torque further. Regarding the difference of the filament creep resistance for the G18 and ET4N filaments, ET4N filaments performed better compared to G18 filaments for small deformations. For the meander filaments with a downwards force direction, the non-sag property of ET4N stood out significantly, as the deformation time was larger than the deformation time of its G18 counterpart by a factor of 9.

The results lead to the final conclusion that the filament design combined with the Lorentz force direction should always prevent the torque reinforcement cycle, which is given for the meander filaments with a downwards force direction. This should also be considered for possible future filament designs. As for the material, the ET4N wire proved to be very resistant to creep processes when no torsion stresses were involved.

The consequence for ITER and other fusion experiments is that, if no superior filament designs are found, the manometers should be equipped with ET4N meander filaments and

a filament wire diameter larger than 0.6 mm. These filaments have to be operated with a heating current direction leading to a downwards-facing Lorentz force on the filament.

In future research on the filaments, dedicated measurements will be repeated several times to test the reproducibility of the deformation processes. Additionally, the dependence of the filament stability on the wire diameter will be experimentally verified and an ideal wire diameter for the filaments will be determined. An analysis of the microscopical structure of the filament materials might be helpful to understand the underlying processes of filament deformation. In further experiments, the connection between heating current, filament temperature and electron emission will be examined, allowing for the evaluation of a critical temperature for creep onset.

Bibliography

[1] U. Stroth. *Plasmaphysik*. 2nd ed. Berlin and Heidelberg, Germany: Springer Spektrum, 2018.

[2] Isabella Milch. *50 Jahre Max-Planck-Institut für Plasmaphysik : Forschung für die Energie der Zukunft*. Online; accessed 21. October 2020. Max-Planck-Institut für Plasmaphysik (IPP), Garching/ Greifswald, 2010. URL: https://www.ipp.mpg.de/ippcms/de/pr/publikationen/buecher/festschrift.

[3] *Photos/Technical*. Online; accessed 31. October 2020. URL: https://www.iter.org/album/Media/7%20-%20Technical.

[4] *What is ITER?* Online; accessed 26. October 2020. URL: https://www.iter.org/proj/inafewlines.

[5] Max Planck Institute for Plasma Physics. *Topical Research*. Online; accessed 30. October 2020. URL: https://www.ipp.mpg.de/10289/stand.

[6] "Neutral pressure and separatrix density related models for seed impurity divertor radiation in ASDEX Upgrade". In: *Nuclear Materials and Energy* 18 (2019), pp. 166–174. ISSN: 2352-1791. URL: http://www.sciencedirect.com/science/article/pii/S2352179118301480.

[7] Alexey Arkhipov et al. "Status of the development of diagnostic pressure gauges for the operation in ITER". In: *Fusion Engineering and Design* 123 (2017), pp. 1049–1053.

[8] Dr. Michael Griener. *At the Plasma Edge*. Online; accessed 29. October 2020. URL: https://www.euro-fusion.org/news/2020/january/at-the-plasma-edge/.

[9] Granville-Phillips. *Introduction to Bayard-Alpert Ionization Gauges*. Online; accessed 20. October 2020. URL: https://mmrc.caltech.edu/Vacuum/Teledyne%20Hastings/Ion%20Gauges.pdf.

[10] U. Wenzel et al. "An ionization pressure gauge with LaB_6 emitter for long-term operation in strong magnetic fields". In: *Review of Scientifc Instruments* 89.033503 (2018).

[11] "Overview of the ITER remote maintenance design and of the development activities in Europe". In: *Fusion Engineering and Design* 136 (2018). Special Issue: Proceedings of the 13th International Symposium on Fusion Nuclear Technology (ISFNT-13), pp. 1117–1124. ISSN: 0920-3796. DOI: https://doi.org/10.1016/j.fusengdes.2018.04.085. URL: http://www.sciencedirect.com/science/article/pii/S0920379618303739.

[12] Alexey Arkhipov et al. "Experimental validation of thermo-mechanical simulations of ITER diagnostic pressure gauges". In: *Fusion Engineering and Design* 136 (2018), pp. 398–402.

[13] ISE. *Wolfram Preis, Vorkommen, Gewinnung und Verwendung*. Online; accessed 15. October 2020. URL: https://institut-seltene-erden.de/seltene-erden-und-metalle/strategische-metalle-2/wolfram/.

[14] Alexey Arkhipov et al. "Mechanical Stability of Filaments for ITER Diagnostic Pressure Gauges Relating to Creep and Fatigue". In: *IEEE Transactions on Plasma Science* 48.6 (2020), pp. 1661–1665.

[15] Nikola Jaksic, Andrea Scarabosio, and Hans Meister. "Pressure gauge filament for neutral gas density measurement using alternating current as source power". In: *Fusion Engineering and Design* 115 (2017), pp. 1–5.

[16] "Pergamon Titles of Related Interest". In: *The Chemistry of Non-Sag Tungsten*. Ed. by L. Bartha et al. Oxford: Pergamon, 1995. ISBN: 978-0-08-042676-1. DOI: https://doi.org/10.1016/B978-0-08-042676-1.50001-4. URL: http://www.sciencedirect.com/science/article/pii/B9780080426761500014.

[17] *Photographs of manometers operated in ASDEX Upgrade made by Dr. Michael Griener*. 2019.

[18] G. Haas and H.S. Bosch. "In vessel pressure measurement in nuclear fusion experiments with ASDEX gauges". In: *Vacuum* 51.1 (1998), pp. 39–46.

[19] Markus Wappl. *Automatization of the calibration process of ASDEX pressure gauges*. Scientific project work at the Technical University Vienna/Max Planck Institute for Plasma Physics Garching (2020).

[20] Max-Planck-Gesellschaft. *Masse des Deuterons korrigiert*. Online; accessed 29. October 2020. URL: https://www.mpg.de/15298233/masse-des-deuterons-korrigiert.

[21] Roman Schwartz and Andreas Lindau. *Das europäische Gravitationszonenkonzept nach WELMEC für eichpflichtige Waagen*. Online; accessed 17. October 2020. Braunschweig. URL: https://www.ptb.de/cms/fileadmin/internet/fachabteilungen/abteilung_1/1.1_masse/1.15/gravzonen.pdf.

[22] J.C. De Vos. "A new determination of the emissivity of tungsten ribbon". In: *Physica* 20.7 (1954), pp. 690–714. ISSN: 0031-8914. DOI: https://doi.org/10.1016/S0031-8914(54)80182-0. URL: http://www.sciencedirect.com/science/article/pii/S0031891454801820.

Appendix A

creep test evaluations

In this section of the appendix, the full evaluation of each creep test is presented. First, the evaluation of the ear filament creep tests are shown, followed by the meander filament creep test evaluation. The evaluation of the creep tests with downwards force direction is always shown first. For each of these configurations, the evaluation of the creep tests with G18 filaments is presented first, followed by the evaluation of the creep tests with ET4N filaments.

A.1 G18 ear filament, downwards force

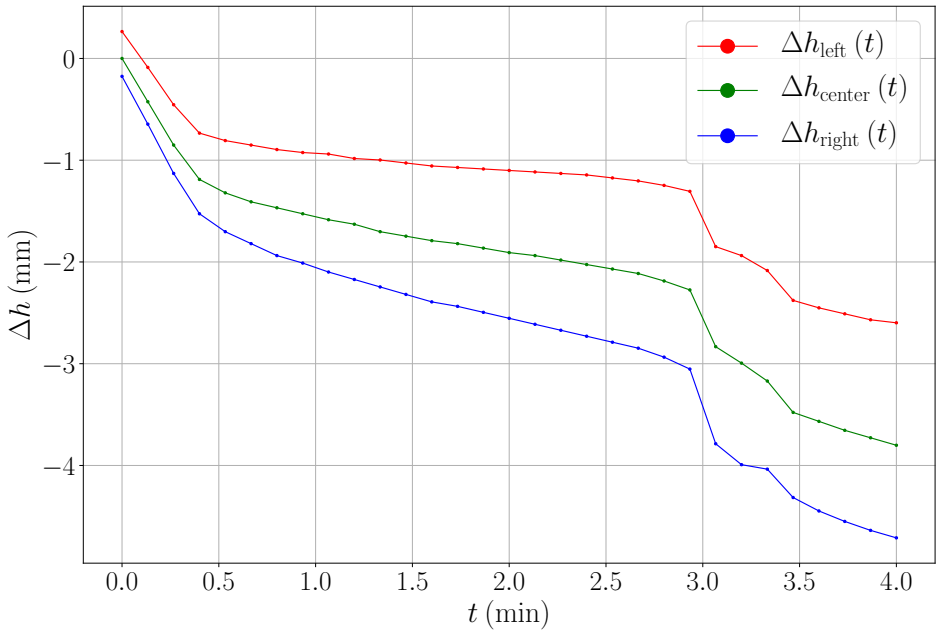

Figure A.1: Evaluation of the front view of a G18 ear filament creep test with a downwards force direction. Height change of the left region of the straight filament section in red, height change in the center in green and height change on the right-hand side in blue.

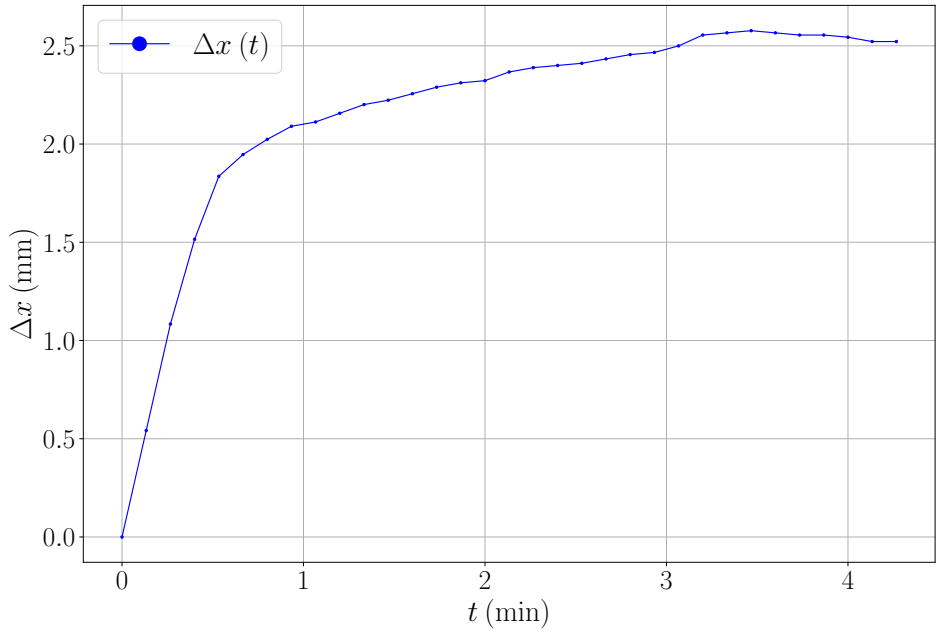

Figure A.2: Evaluation of the side view of a G18 ear filament creep test with a downwards force direction. The blue curve shows the width change of the filament. Large change in filament width due to unfolding of the filament.

A.2 ET4N ear filament, downwards force

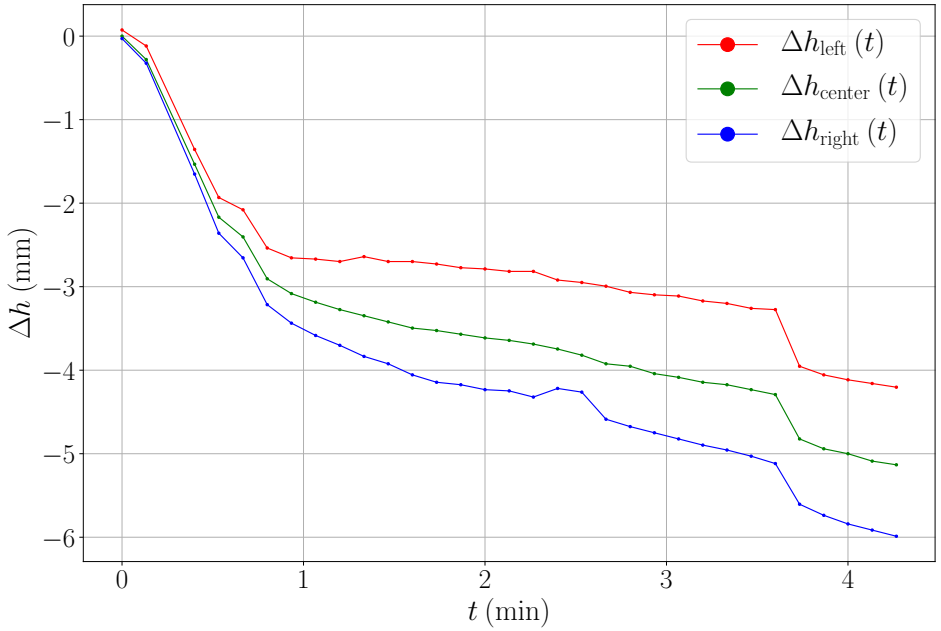

Figure A.3: Evaluation of the front view of an ET4N ear filament creep test with a downwards force direction.

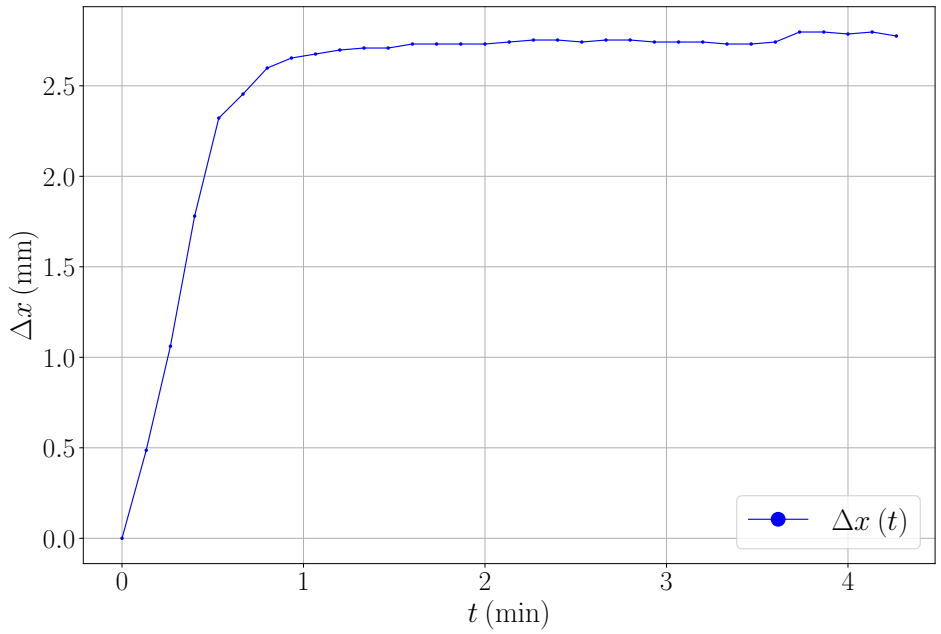

Figure A.4: Evaluation of the side view of an ET4N ear filament creep test with a downwards force direction.

A.3 G18 ear filament, upwards force

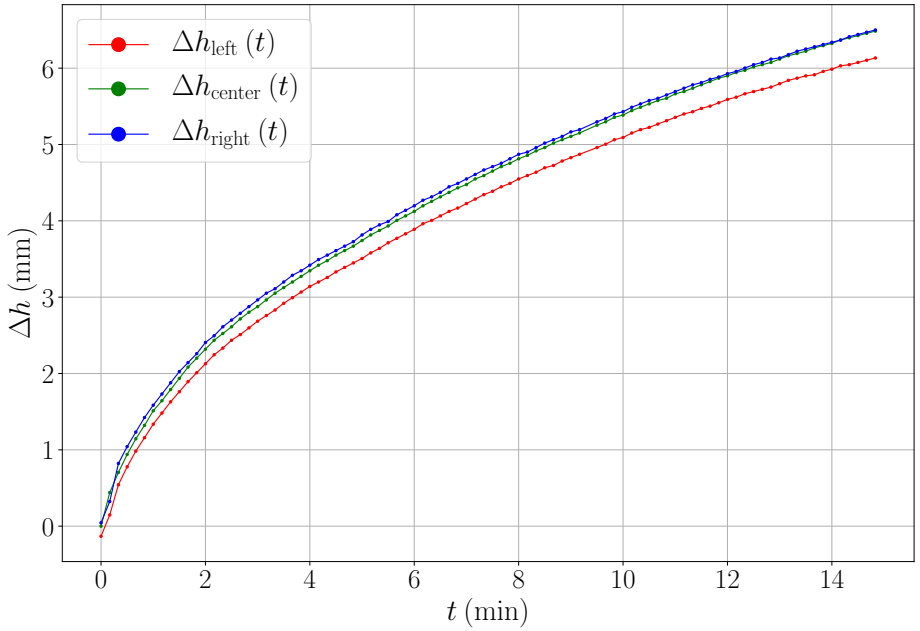

Figure A.5: Evaluation of the front view of a G18 ear filament creep test with an upwards force direction.

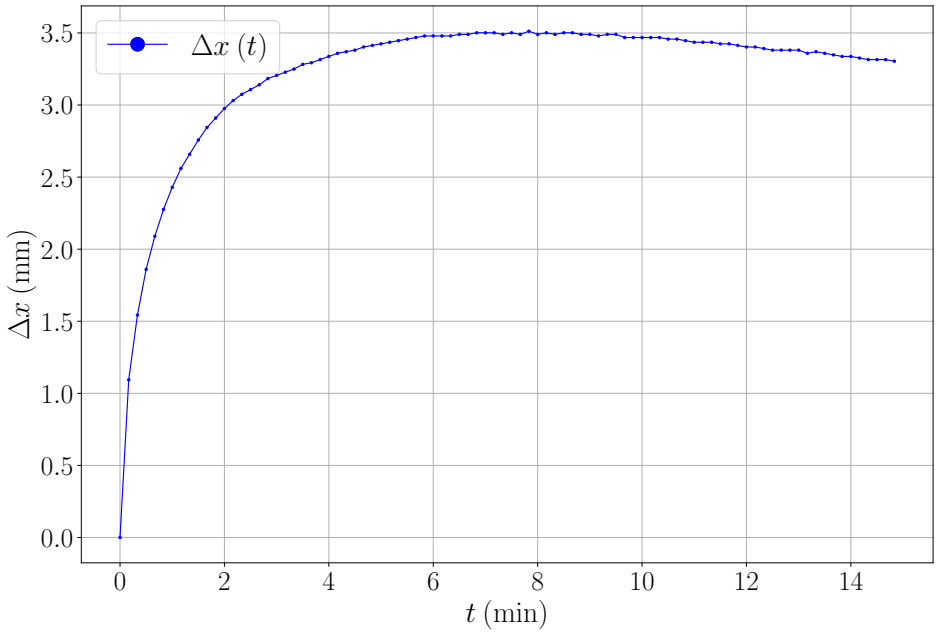

Figure A.6: Evaluation of the side view of a G18 ear filament creep test with an upwards force direction. The blue curve shows the width change of the filament.

A.4 ET4N ear filament, upwards force

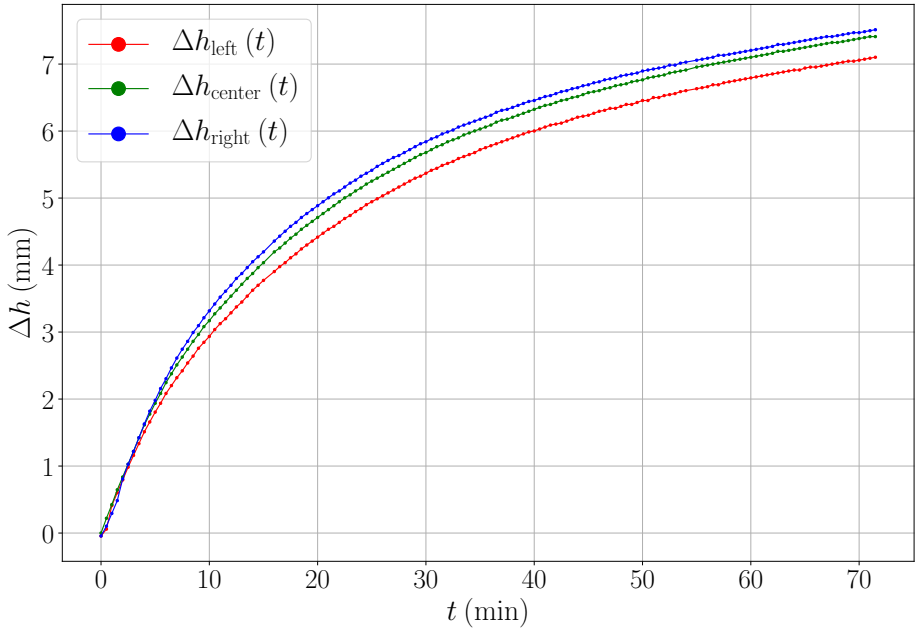

Figure A.7: Evaluation of the front view of an ET4N ear filament creep test with an upwards force direction.

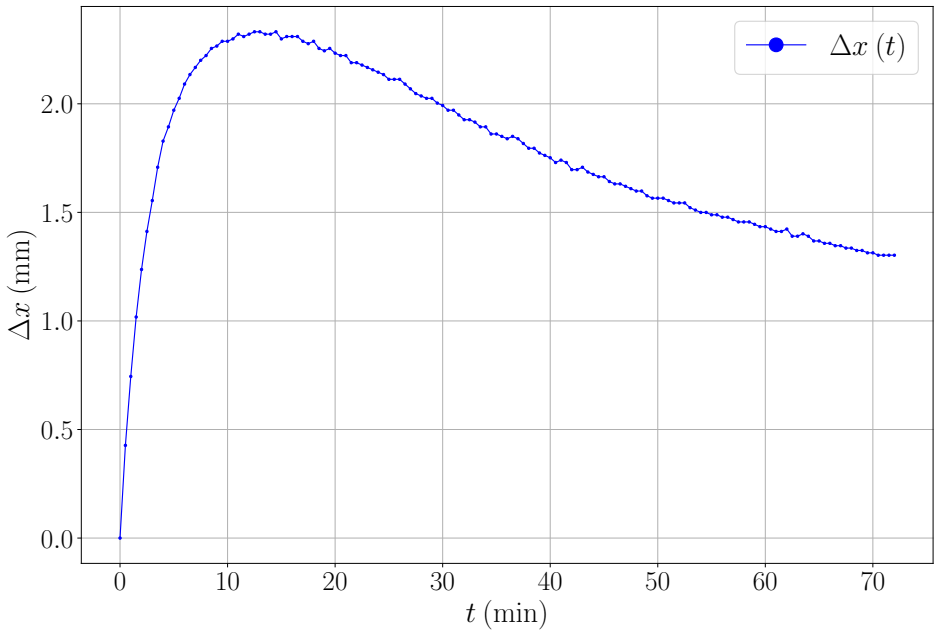

Figure A.8: Evaluation of the side view of an ET4N ear filament creep test with an upwards force direction.

A.5 G18 meander filament, downwards force

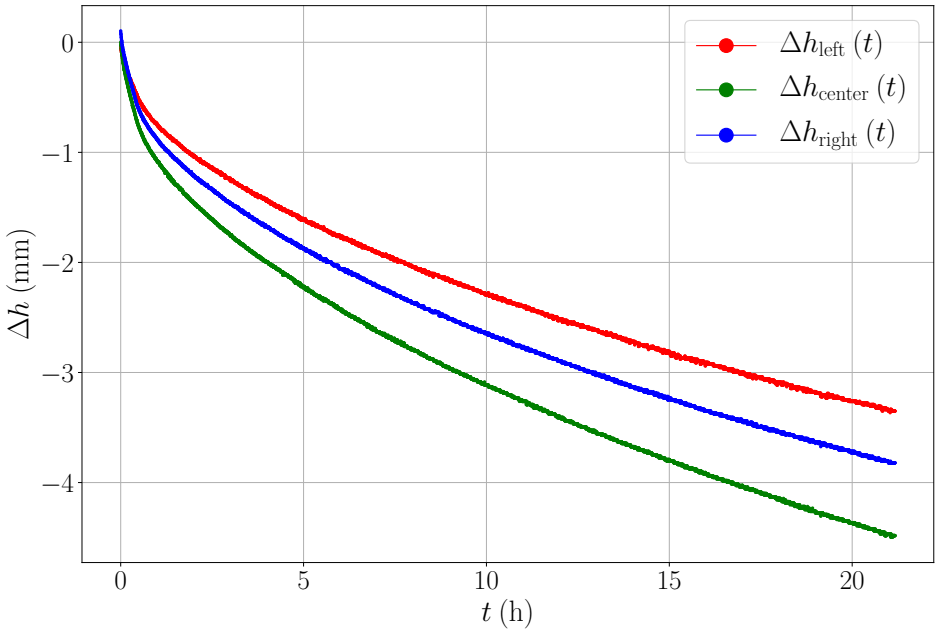

Figure A.9: Evaluation of the front view of a G18 meander filament creep test with a downwards force direction.

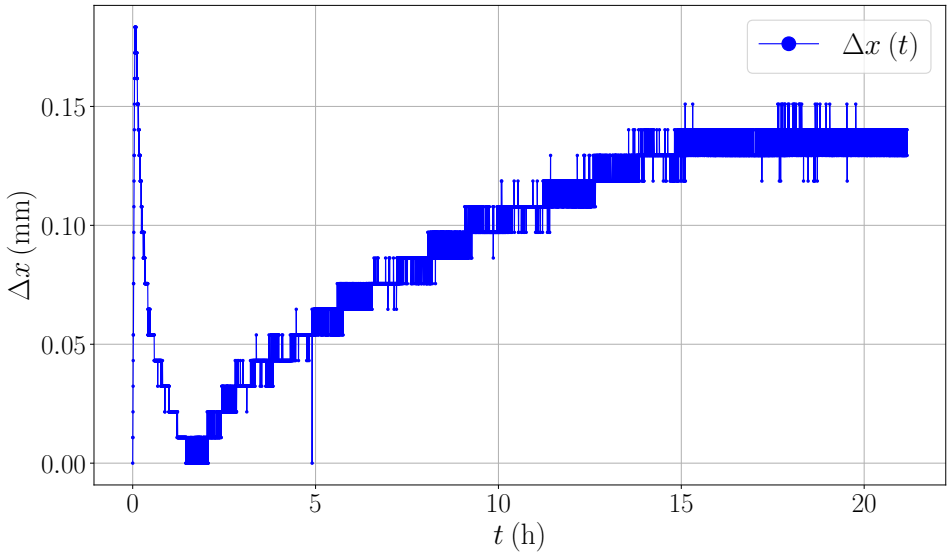

Figure A.10: Evaluation of the side view of a G18 meander filament creep test with a downwards force direction. Almost no change in filament width, the filament keeps its planar shape. The maximal resolution of the evaluation is visible, as the distance between two pixels corresponds to 11 µm.

A.6 ET4N meander filament, downwards force

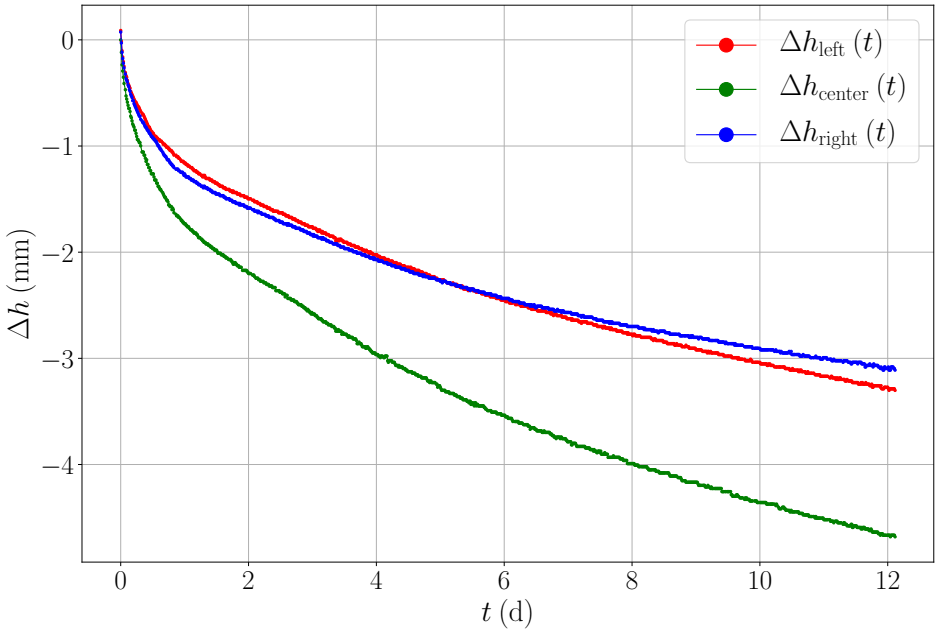

Figure A.11: Evaluation of the front view of an ET4N meander filament creep test with a downwards force direction.

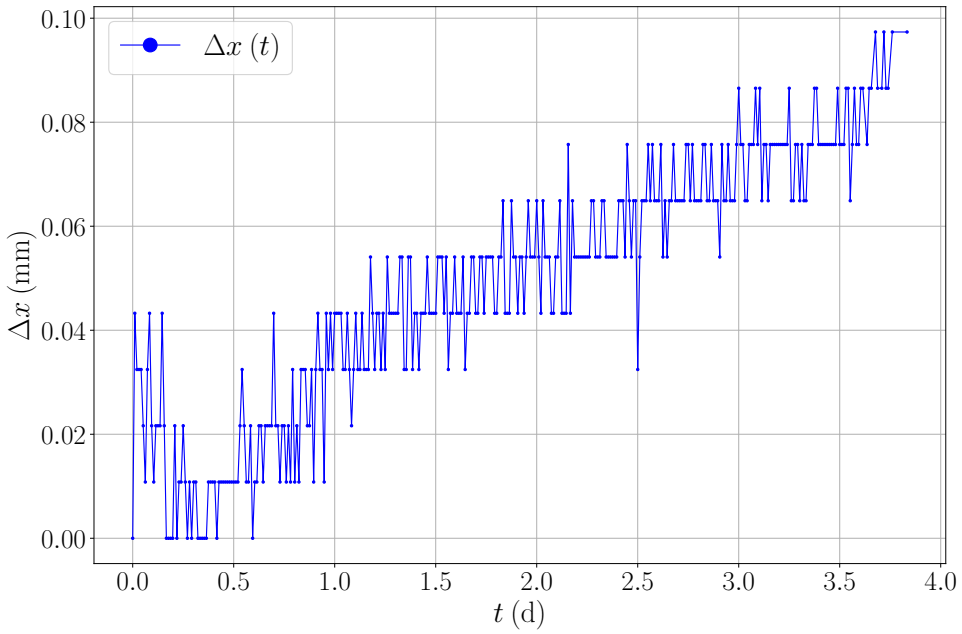

Figure A.12: Evaluation of the side view of an ET4N meander filament creep test with a downwards force direction.

A.7 G18 meander filament, upwards force

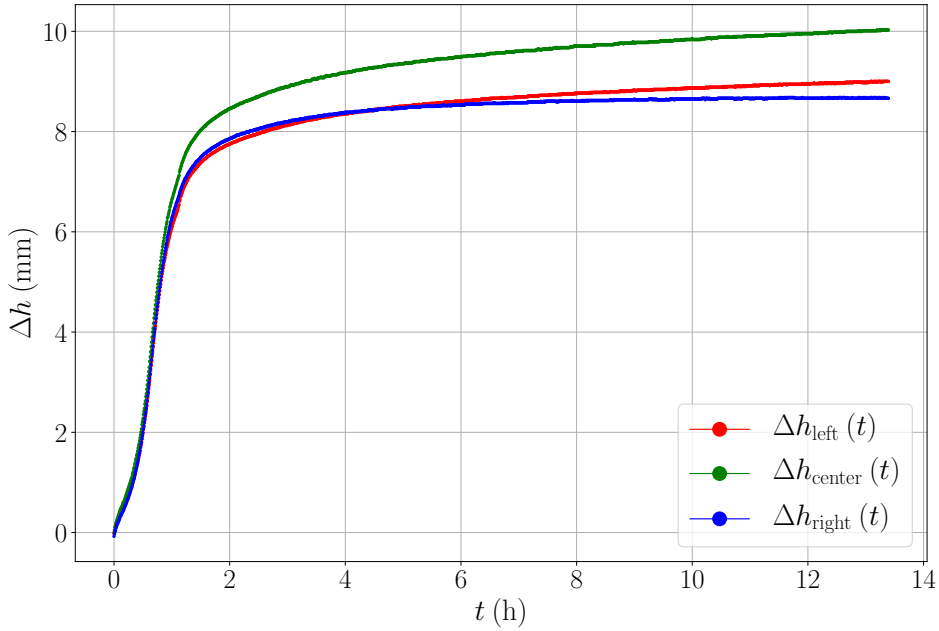

Figure A.13: Evaluation of the front view of a G18 meander filament creep test with an upwards force direction.

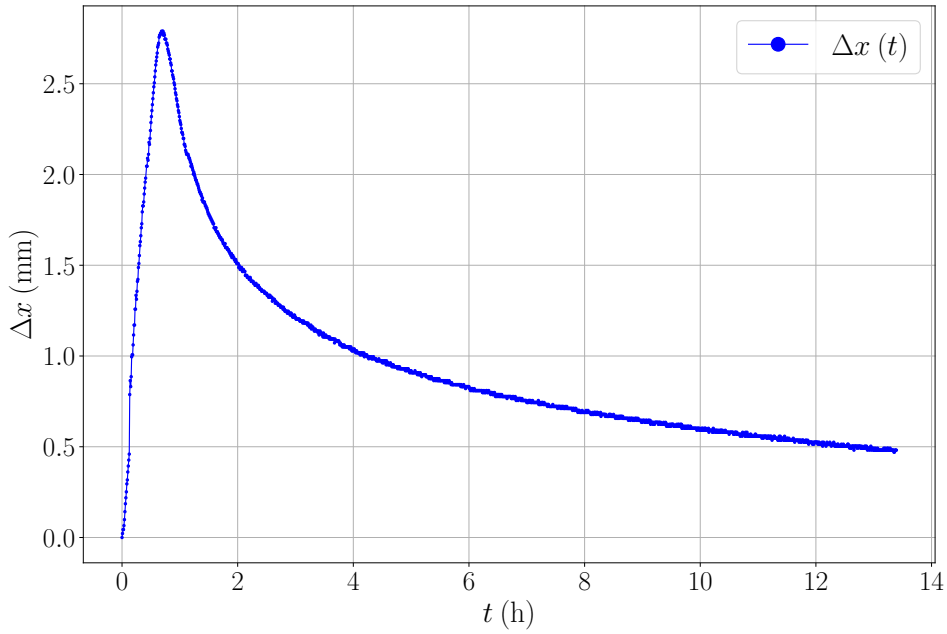

Figure A.14: Evaluation of the side view of a G18 meander filament creep test with an upwards force direction.

A.8 ET4N meander filament, upwards force

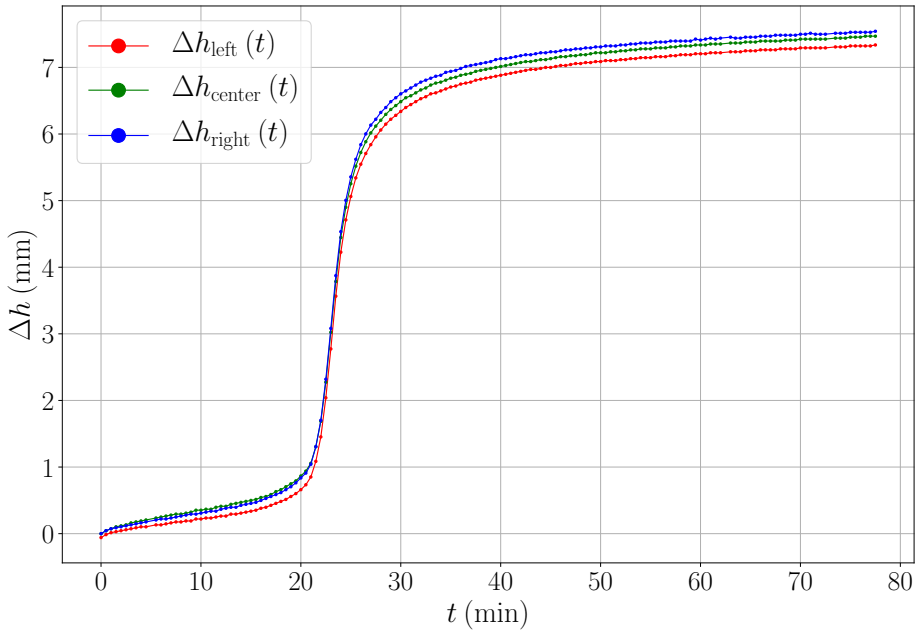

Figure A.15: Evaluation of the front view of an ET4N meander filament creep test with an upwards force direction. Torque reinforcement cycle visible in the first 20 min to 30 min of the experiment.

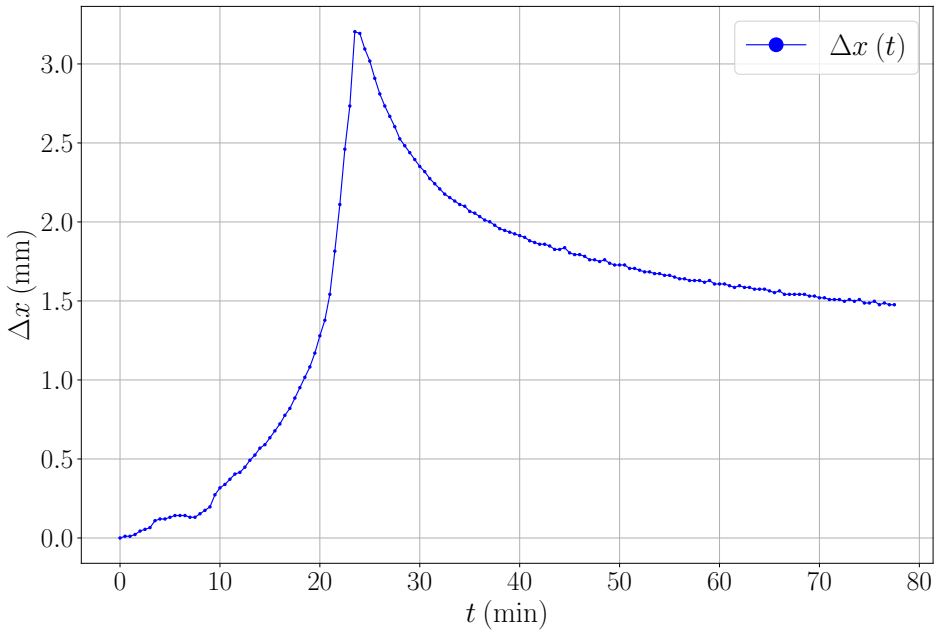

Figure A.16: Evaluation of the side view of an ET4N meander filament creep test with upwards force direction. Torque reinforcement cycle visible in the first 20 min to 30 min of the experiment. Large increase in filament width in approximately the first 24 min, followed by a large decrease of the filament width. The peak marks the point, at which the cycle ends.

Erklärung

Hiermit erkläre ich, dass die vorliegende Bachelorarbeit von mir selbstständig verfasst wurde, und dass keine anderen als die angegebenen Hilfsmittel benutzt wurden. Die Stellen der Arbeit, die anderen Werken dem Wortlaut oder Sinn nach entnommen sind, sind in jedem einzelnen Fall unter Angabe der Quelle als Entlehnung kenntlich gemacht. Diese Erklärung erstreckt sich auch auf etwa in der Arbeit enthaltene Grafiken, Zeichnungen, Kartenskizzen und bildliche Darstellungen.